

19 Abstract

20 The biological oxygen (O_2) saturation anomaly ($\Delta O_2/Ar$) is a tracer for net community
21 production (NCP) in marine surface waters, with argon (Ar) normalization used to correct for
22 physical effects on O_2 supersaturation. Ship-board mass spectrometry has been used for $\Delta O_2/Ar$
23 measurements, but this approach may not be accessible to many research groups. Here, we
24 present a proof-of-concept for NCP estimates based on underway measurements of $\Delta O_2/N_2$,
25 which can be obtained from deployments of O_2 -Optodes and gas tension devices (GTD). We
26 used a one-dimensional mixed layer model, validated against field observations, to evaluate
27 divergence in $\Delta O_2/Ar$ and $\Delta O_2/N_2$ resulting from differences in the sensitivity of Ar and nitrogen
28 (N_2) to various physical processes. Changes in sea surface temperature and responses in air-sea
29 exchange most strongly decouple surface Ar and N_2 , with additional excess N_2 associated with
30 bubble-injection during high-wind conditions and vertical mixing in regions of elevated
31 subsurface N_2 . In contrast, biological N_2 -fixation has a negligible contribution to the observed
32 divergence between Ar and N_2 . Based on readily available environmental data, we present an
33 approach to correct for Ar and N_2 differences, yielding a new tracer, N_2' , that is a near analog of
34 Ar. We show that $\Delta O_2/N_2'$ provides an excellent approximation to $\Delta O_2/Ar$, and that uncertainty
35 and biases in $\Delta O_2/N_2'$ are small relative to other errors in NCP calculations. Our results
36 demonstrate the potential for $\Delta O_2/N_2'$ measurements to expand NCP estimates from
37 oceanographic research surveys, vessels of opportunity or autonomous surface vehicles.

38

39 Plain Language Summary

40 Marine net community production, NCP, represents the difference between biological oxygen
41 (O_2) production through photosynthesis and O_2 consumption through respiration. This quantity
42 reflects the ocean's capacity to support marine life and remove carbon dioxide from the
43 atmosphere. One common approach to estimate NCP employs mass spectrometry to measure the
44 oxygen-to-argon ratio ($\Delta O_2/Ar$) in surface seawater. Since Ar is biologically inert and has similar
45 physical properties to O_2 , this approach is used to examine marine biological production.
46 However, the instrumentation required to measure $\Delta O_2/Ar$ is expensive and requires significant
47 technical oversight, thus limiting the coverage of observations. Here, we use simple numerical
48 simulations to show that NCP can be accurately derived from the seawater O_2 -to-nitrogen ratio
49 ($\Delta O_2/N_2$). We derive a new term, $\Delta O_2/N_2'$, that corrects for small differences between $\Delta O_2/N_2$
50 and $\Delta O_2/Ar$ resulting from the enhanced sensitivity of N_2 to bubbles, seawater temperature
51 changes and mixing effects. NCP calculated from $\Delta O_2/N_2'$ provides an excellent alternative to
52 $\Delta O_2/Ar$ -based estimates, and uncertainty in $\Delta O_2/N_2'$ is low relative to other error sources in NCP
53 calculations. As $\Delta O_2/N_2$ can be measured autonomously at sea with simple instrumentation, our
54 results demonstrate the potential to expand coverage of NCP estimates from a variety of
55 sampling platforms.

56

57 1 Introduction

58 Net community production (NCP) quantifies the balance between gross photosynthetic
59 production and community-wide respiration, and serves as an important metric of the metabolic
60 state of an ocean region. Integrated over seasonal timescales, NCP constrains upper limits on
61 marine biomass production and carbon export from the ocean surface via the biological pump.

62 As such, the spatial and temporal distribution of marine NCP has significant implications for
 63 food web dynamics and global biogeochemical cycles. To understand and predict the response of
 64 marine systems to future environmental change, it is therefore important to quantify NCP on
 65 ecologically-relevant time and space scales.

66 An increasingly common approach for deriving oceanic NCP estimates at high spatial
 67 resolution employs ship-based mass spectrometry to obtain underway measurements of the
 68 seawater oxygen-to-argon ratio (O_2/Ar). This approach relies on the nearly identical solubility
 69 properties of O_2 and its biologically-inert analog Ar, which make O_2/Ar largely insensitive to
 70 temperature or salinity-dependent solubility changes, or bubble injection processes (Craig &
 71 Hayward, 1987; Fig. S1). The biological saturation anomaly ($\Delta O_2/Ar$, Eq. 1) thus provides a
 72 specific tracer for net biological O_2 production, and can be derived by normalizing measured
 73 O_2/Ar ($[O_2/Ar]_{sw}$) to the seawater equilibrium ratio ($[O_2/Ar]_{eq}$).

$$74 \quad \Delta O_2/Ar = \left(\frac{[O_2/Ar]_{sw}}{[O_2/Ar]_{eq}} - 1 \right) \cdot 100 \% \quad (1)$$

75 Net community production is then equated to the air-sea flux of biologically-produced excess O_2
 76 (i.e. the “bioflux” of $\Delta O_2/Ar \cdot [O_2]_{eq}$; Jonsson et al., 2013; Kaiser et al., 2005; Teeter et al.,
 77 2018). This approach has been applied to obtain broad spatial coverage of NCP estimates from
 78 ship-based surveys, thus improving our understanding of marine carbon cycling (e.g. Hamme et
 79 al., 2012; Howard et al., 2010; Izett et al., 2018; Juranek et al., 2019; Lockwood et al., 2012;
 80 Rosengard et al., 2020; Tortell et al., 2015; Ulfso et al., 2014). However, the expense of mass
 81 spectrometers and the technical expertise required to run these instruments may be prohibitive to
 82 some research groups. Additionally, mass spectrometers can have significant power consumption
 83 requirements and are generally not capable of fully-autonomous deployments, thus limiting their
 84 use to scientific research vessels with dedicated infrastructure and personnel. Truly autonomous
 85 gas measurements on ships of opportunity, or in-situ platforms such as autonomous surface
 86 vehicles (e.g. Saildrone), would significantly expand the global coverage of NCP estimates from
 87 underway surveys, helping to integrate these measurements with a growing suite of autonomous
 88 biogeochemical and ecological observations (Gordon et al., 2020; Johnson et al., 2017; Mordy et
 89 al., 2017; Pelland et al., 2018; Plant et al., 2016; Yang et al., 2017).

90 The development of O_2 Optodes (Tengberg et al., 2006) and Gas Tension Devices
 91 (GTDs; McNeil et al., 2006a; Reed et al., 2018) capable of stable, accurate measurements during
 92 extended in-situ deployments provides new opportunities for autonomous NCP surveys. Using
 93 observations of O_2 from the Optode and the seawater total dissolved gas pressure (i.e. the sum of
 94 all gas partial pressures) from the GTD, it is possible to obtain estimates of seawater nitrogen
 95 (N_2) concentrations (McNeil et al., 1995). Nitrogen has roughly similar physical properties to O_2
 96 (i.e. salinity and temperature solubility dependence; Fig. S1), such that NCP could, in principle,
 97 be approximated from N_2 -based calculations of the biological O_2 saturation anomaly (i.e.
 98 $\Delta O_2/N_2$, following Eq. 1).

99 To date, O_2 and N_2 measurements have been combined to estimate NCP time-series from
 100 Optode and GTD deployments on moorings and/or floats (e.g. Bushinsky & Emerson, 2015;
 101 Emerson & Stump, 2010; Weeding & Trull, 2014; Yang et al., 2017). These applications employ
 102 simultaneous observations of sea surface temperature, salinity and wind speed to estimate the
 103 contribution of physical processes driving changes in O_2 solubility, thereby isolating a biological
 104 signature of NCP without the need for Ar or N_2 normalization. In these studies, mooring-based

105 N₂ measurements are commonly used to estimate the effects of physical processes on the mixed
 106 layer O₂ budget, most importantly air-sea flux via bubbles (Emerson et al., 2019). Thus far,
 107 direct estimates of NCP from O₂ and N₂ measurements have only been obtained from ship-based
 108 depth profiles (McNeil et al., 2006b) or in-ice measurements (Zhou et al., 2014). To our
 109 knowledge, no previous work has derived NCP from underway surface $\Delta\text{O}_2/\text{N}_2$, although Tortell
 110 et al. (2015) used simultaneous O₂/N₂ and O₂/Ar data to describe physical and biological controls
 111 on O₂ across various hydrographic regimes in the Southern Ocean.

112 A key challenge in the use of $\Delta\text{O}_2/\text{N}_2$ measurements as an NCP tracer is accounting for
 113 divergences in mixed layer $\Delta\text{O}_2/\text{Ar}$ and $\Delta\text{O}_2/\text{N}_2$ resulting from the slightly different solubility
 114 properties of Ar and N₂ (Fig. S1). Nitrogen is less soluble in water than O₂ and Ar, and is
 115 therefore more susceptible to bubbled-induced supersaturation (Craig & Hayward, 1987; Weiss,
 116 1970; Woolf & Thorpe, 1991). Moreover, small differences in the temperature-sensitivity of
 117 O₂/Ar and O₂/N₂ induce differential responses to surface warming or cooling. Finally, N₂, unlike
 118 Ar, is not entirely inert, as its concentration can be altered by N₂-fixation, denitrification, and
 119 anammox. If differences between Ar and N₂ supersaturation anomalies (ΔAr and ΔN_2 ,
 120 respectively) are sufficiently large and unaccounted for, interpretations of NCP estimated from
 121 $\Delta\text{O}_2/\text{N}_2$ could be biased, with significant implications for the interpretation of oceanic net tropic
 122 status and metabolic state.

123 The primary goal of this article is to demonstrate the utility of $\Delta\text{O}_2/\text{N}_2$ measurements as
 124 an alternative to $\Delta\text{O}_2/\text{Ar}$ for NCP estimates. We present simulations from a simple one-
 125 dimensional model, validated against in-situ N₂ and O₂ measurements, to evaluate differences
 126 between $\Delta\text{O}_2/\text{Ar}$ and $\Delta\text{O}_2/\text{N}_2$ resulting from ΔAr and ΔN_2 divergence in surface waters. Based on
 127 the simulations, we tested a framework for predicting these differences from readily-available
 128 environmental data, and derived a new tracer, N₂' ("N₂-prime"), which accounts for excess ΔN_2
 129 relative to ΔAr . We conclude by evaluating the uncertainty in NCP calculations based on
 130 $\Delta\text{O}_2/\text{N}_2'$ measurements. Our results demonstrate the potential for underway, ship-based
 131 observations of $\Delta\text{O}_2/\text{N}_2$ (and derived $\Delta\text{O}_2/\text{N}_2'$) to expand coverage of NCP estimates in oceanic
 132 waters. In the supporting information (SI), we provide details and software code for the
 133 application of the N₂' approach to field surveys. In related articles (Izett & Tortell, 2020) we
 134 describe an underway measurement system for ship-board O₂/N₂ surveys, and provide a field-
 135 validation of the approach proposed here (manuscript in preparation).

136

137 2 Methods

138 2.1 One-dimensional mixed layer physical gas model

139 We developed a simple one-dimensional mixed layer box model to evaluate mechanisms
 140 driving the divergence between ΔAr and ΔN_2 under various environmental forcing conditions
 141 (i.e. $\Delta C = (C/C_{\text{eq}} - 1) * 100 \%$, where C_{eq} is the equilibrium solubility concentration at ambient
 142 sea level pressure). We also tested an empirical approach for correcting these offsets, which is
 143 described in section 2.2. The model predicts the evolution of mixed layer gas concentrations
 144 resulting from physical perturbations, including temperature-dependent solubility changes, air-
 145 sea exchange, and vertical mixing. The following budget was applied to O₂, Ar and N₂:

$$146 \quad \text{MLD} \cdot \frac{dC}{dt} = F_d + F_B + F_M. \quad (2)$$

147 Here, MLD is the mixed layer depth, dC/dt is the change in gas concentration over time,
148 F_A and F_B are the air-sea gas exchange fluxes via diffusion and bubbles (from both fully- and
149 partially-collapsing bubbles), respectively, and F_M represents the sum of diapycnal mixing,
150 upwelling and entrainment of water from below the mixed layer. We employ a two-box domain,
151 with prescribed hydrographic properties in the subsurface and mixed layers (see below). Unless
152 otherwise stated, we excluded biological production of O_2 and N_2 and ignored lateral fluxes (see
153 below).

154 We used the air-sea exchange parameterization of Liang et al. (2013) in ice-free
155 simulations. For Arctic simulations (fractional ice cover $>1\%$) we excluded explicit bubble
156 fluxes, but scaled bulk gas exchange rates with the fraction of ice-free water following
157 Butterworth & Miller (2016). Net air-sea exchange fluxes differ by less than 5% between these
158 two parameterizations at wind speeds below $\sim 10\text{ m s}^{-1}$, thus justifying our exclusion of bubble
159 processes in waters with $>1\%$ ice coverage. We note that the time-series of N_2 and Ar predicted
160 by our simulations, and the relative differences between them, will depend on the air-sea
161 diffusion rates of these gases applied in our model domain. The Liang et al. (2013) bubble-
162 mediated flux model is based on Ar diffusion rates which are believed to exceed those of N_2
163 (Fig. S1). There is, however, some disagreement in the literature, with suggestions that N_2
164 diffusion may exceed Ar (e.g. Wise & Houghton, 1966). Nonetheless, the results presented here
165 are consistent with the majority of studies describing surface diffusion rates (e.g. see within
166 Wanninkhof, 2014), and the Liang et al. model has been validated for N_2 and other similar gases
167 (Emerson & Bushinsky 2016; and see below, section 3.3). The analyses presented throughout
168 this manuscript are thus based on the assumption that Ar diffusion rates exceed those of N_2 .

169 The mixing flux term encompasses diapycnal mixing, upwelling and entrainment, and is
170 proportional to the vertical gas gradient (i.e. $dC/dZ = (C_{\text{deep}} - C_{\text{surf}}) / dZ$, where C_{deep} is the
171 subsurface gas concentration). Terms for these fluxes are derived from a prescribed eddy
172 diffusivity coefficient (κ_z), Ekman pumping velocity (ω , proportional to wind speed; Hartmann,
173 1994) and the rate of MLD deepening ($d\text{MLD}/dT$), respectively. These parameterizations are
174 described briefly below, with full details presented in section S1 of the SI. Model code for
175 performing simulations is also provided at doi.org/10.5281/zenodo.4024952.

176 We performed sensitivity analyses comparing our simulated gas time-series with in-situ
177 observations (see below section 3.3) to determine appropriate parameterizations for the bubble
178 scaling factor, β , and the integration depth scale, dZ , over which vertical mixing fluxes are
179 estimated.

180 From these analyses, we found that a bubble flux scaling coefficient, β , of 0.5 produces
181 best results, and is consistent with results from Yang et al. (2017) and Emerson et al. (2019). A
182 vertical mixing depth scale, dZ , proportional to the thermocline depth, is also most appropriate,
183 but is generally insensitive to small variability (e.g. $\pm 10\text{ m}$). In the experimental simulations, dZ
184 was set to a constant value (25 m) based on an empirical relationship between MLD and the
185 thermocline depth.

186 The model was initialized and forced with either real observations or simulated values, as
187 described below. Unless otherwise stated, sea level pressure (SLP), salinity and MLD were held
188 constant, and gas concentrations were initialized at 100% saturation using the solubility
189 equations of Garcia & Gordon (1993) and Hamme & Emerson (2004). Subsurface Ar ($\Delta\text{Ar}_{\text{deep}}$)
190 was set based on previously published observations, and $\Delta\text{N}_{2,\text{deep}}$ was varied in each model run

191 by adjusting subsurface $\Delta N_2/Ar$ (i.e. $\Delta N_2/Ar_{deep} = (N_{2,sat,deep} / Ar_{sat,deep} - 1) \cdot 100 \%$). Our
192 simulations neglect lateral fluxes as they are generally small in a Eulerian framework, and
193 irrelevant to underway surveys which measure gas concentrations that have been modified along
194 a Lagrangian flow path (Teeter et al., 2018).

195

196 2.1.1 Model simulations

197 We performed six simulations with our gas model to examine the main drivers of ΔAr
198 and ΔN_2 divergence. Table 1 summarizes the different forcing conditions used for these
199 simulations. For all model runs, we performed calculations in 0.25-day time increments, and
200 omitted the first 90 days of output so that the simulated results were independent of initial
201 conditions. Four of the simulations (denoted as ‘experimental’ and named with the prefix ‘Ex’)
202 were designed to represent the impacts of extreme temperature (SST) and wind speed (u_{10})
203 variability in ice-free (runs Ex-IF 1, Ex-IF 2, and Ex-IF 3) and partially ice-covered (run Ex-IC
204 1) waters. Two additional simulations (denoted as ‘realistic’ and named with the prefix ‘real’)
205 included more realistic environmental forcing, based on in-situ observations at Ocean Station
206 Papa in the Subarctic Pacific (real-OSP) and Baffin Bay (real-BB) in the eastern Arctic,
207 respectively.

208 In the experimental runs, initial conditions (temperature and salinity profiles) were
209 derived from representative 2019 observations from Ocean Station Papa (50 °N, 145 °W; runs
210 Ex-IF 1–3) and northern Baffin Bay (67 °N, 62.5 °W; Ex-IC 1) (data provided by the Institute of
211 Ocean Sciences, DFO Canada at www.waterproperties.ca/linep and by Amundsen Science Data
212 Collection, 2019 at www.polardata.ca). To simulate extreme environmental change, we
213 introduced two rapid step-changes in u_{10} (between 7 and 15 m s⁻¹) and SST (± 4 °C) based on
214 observed variability in Subarctic NE Pacific and Arctic field studies (R. Izett and P. Tortell
215 unpublished results). Mixed layer depth, salinity, subsurface properties and dZ were derived
216 from the initial conditions and held constant throughout the run. For each set of conditions, we
217 performed three runs (details in Table 1): (a) no mixing; (b) dampened mixing; (c) full mixing.
218 For runs b and c, we prescribed κ_Z values and scaled ω (upwelling velocity) with u_{10} .
219 Entrainment was set to zero, because the MLD was constant. We set the value of $\Delta N_2/Ar_{deep}$ to
220 1.5 % in the experimental simulations based on the observed upper range of $\Delta N_2/Ar$ just below
221 the mixed layer in most ocean basins (e.g. Hamme et al., 2017, 2019; Hamme & Emerson, 2013;
222 Nicholson et al., 2010). Although subsurface $\Delta N_2/Ar_{deep}$ can range from $<0 \%$ to $>2 \%$ (Chang et
223 al., 2010, 2012; Hamme et al., 2019; Shigemitsu et al., 2016), values greater than $\sim 1.5 \%$ are rare
224 outside of tropical and sub-tropical zones impacted by near-surface water column denitrification.

225 In the realistic simulations, u_{10} and SST data were obtained from in-situ mooring
226 observations (real-OSP) or gridded reanalysis products (real-BB). In the Subarctic Pacific runs,
227 we approximated a two year cycle (2011-2013) using u_{10} , SST and SLP data from the NOAA
228 PMEL mooring at OSP (provided by NOAA PMEL at www.pmel.noaa.gov). For the Baffin Bay
229 simulations (representing May – October, 2019), u_{10} data were obtained from the CCMP vector
230 product (provided by Remote Sensing Systems at www.remss.com/measurements/ccmp/; Atlas
231 et al., 2011), while SST and sea ice percent-coverage were from the NOAA High Resolution OI
232 Dataset (provided by NOAA ESRL at psl.noaa.gov; Reynolds et al., 2007) and SLP was from the
233 NCEP/NCAR reanalysis 2 product (provided by NOAA ESRL at psl.noaa.gov; Kalnay et al.,
234 1996). In both realistic simulations, we applied a time-variable MLD based on density

235 measurements obtained on the OSP mooring line (real-OSP), or from the NOAA MIMOC mixed
236 layer depth climatology (real-BB; provided by NOAA PMEL at pmel.noaa.gov/mimoc;
237 Schmidtko et al., 2013). We performed two simulation runs representing different mixing
238 scenarios (Table 1), omitting the weak mixing scenario (i.e. run b). In run c of the OSP
239 simulation (i.e. full mixing), we applied time-varied κ_z by extrapolating the results from Cronin
240 et al. (2015) onto our model domain. In real-BB run c, time-variable κ_z was set based on eddy
241 diffusivity values obtained from NEMO model simulations of the Arctic and N. Atlantic (NEMO
242 model simulations described in Castro de la Guardia et al., 2019). Subsurface gases were set
243 based on calculated equilibrium concentrations at the deep temperature and salinity conditions,
244 and from supersaturation anomalies based on archived observations below the MLD in the
245 subarctic Pacific and Labrador Sea (provided at www.bco-dmo.org; Hamme et al., 2019). In real-
246 OSP run c, ΔA_{deep} and $\Delta N_2/A_{\text{deep}}$ were interpolated from observations from multi-year sampling
247 at OSP in February, June and August to the model run time (ranges 0-1 % and 0-0.5 %,
248 respectively). In real-BB run c, ΔA_{deep} and $\Delta N_2/A_{\text{deep}}$ were held constant 0 % and 0.5 %,
249 respectively. Temperature, salinity and O_2 in the “deep” boxes (i.e. the layer beneath the MLD)
250 were based on observations at the OSP mooring (real-OSP) or from profile measurements and
251 NEMO model output in northern Baffin Bay (real-BB). In the real-OSP and real-BB simulations,
252 we applied biological production terms to the O_2 budget (Eq. 2) based on field observations from
253 the respective regions to better reflect seasonal ΔO_2 variability (mean annual cycle at OSP from
254 Fassbender et al., 2016 and constant NCP in BB from on R. Izett and P. Tortell unpublished
255 results).

256

257

258 **Table 1.** Summary of model simulation conditions. Vertical advection and entrainment fluxes
 259 were set to zero in run a of all simulations, and were proportional to wind speed and the rate of
 260 MLD deepening in runs b and c, respectively. Initial conditions were obtained from ship-based
 261 observations at Ocean Station Papa (OSP) in the Subarctic Pacific, NOAA mooring data at OSP,
 262 or ship-based measurements in Baffin Bay (BB). The three numbers listed for SST and u_{10}
 263 correspond with values used during each of three forcing time segments (days 0-12, 12-65, and
 264 65-1 20 in Fig. 1). In the real-OSP and real-BB run c, we derived time-variable κ_z from Cronin et
 265 al. (2015) and NEMO model simulations, respectively, while $\Delta N_2/Ar_{\text{deep}}$ was based on archived
 266 values from Hamme et al. (2019). Both terms were set to zero in run a of the realistic
 267 simulations. We did not perform intermediate mixing scenarios (i.e. run b) for the realistic
 268 simulations. The results of these simulations are shown in Figs. 2-4.

Simulation (duration)	Forcing					Mixing	
	deep & initial conditions	SST [°C]	u_{10} [m s ⁻¹]	ice [%]	SLP [mbar]	κ_z [m ² s ⁻¹]	$\Delta N_2/Ar_{\text{deep}}$ [%]
Ex-IF 1 (120 days)	OSP profile	10, 10, 10	7, 15, 7	0	1013.25		
Ex-IF 2 (120 days)	OSP profile	10, 14, 10	7, 7, 7	0	1013.25	Run a: 0 Run b: 10 ⁻⁵ Run c: 10 ⁻⁴	Run a: 0 Run b: 1.5 Run c: 1.5
Ex-IF 3 (120 days)	OSP profile	6, 10, 14	7, 15, 7	0	1013.25		
Ex-IC 1 (120 days)	BB profile	0, 4, 8	7, 15, 7	50	1013.25		
real-OSP (Jan. 2011- Jan. 2013)	NOAA OSP mooring profile	NOAA OSP mooring	NOAA OSP mooring	0	NOAA OSP mooring	Run a: 0 Run c: Cronin	Run a: 0 Run c: Hamme
real-BB (May – Oct. 2019)	BB profile	NOAA OI SST product	CCMP product	NOAA OI ice product	NCEP/ NCAR reanalysis	Run a: 0 Run c: NEMO	Run a: 0 Run c: 0.5

270

271 2.2 Derivation of N_2'

272 Based on our simulations, we developed a framework to reconcile the differences
 273 between surface water $\Delta O_2/Ar$ and $\Delta O_2/N_2$ resulting from differential solubility effects and
 274 physical fluxes of Ar and N_2 . From this analysis, we derived a new tracer, N_2' (“ N_2 -prime”) that
 275 corrects for these differences and provides an Ar analog. For this approach, we used a slightly
 276 simplified version of the gas budget described in Eq. 2 to predict the difference between ΔN_2 and
 277 ΔAr occurring over a timescale relevant to NCP calculations. We then subtracted this estimated
 278 offset from ΔN_2 derived from the full model simulations. We modified Eq. 2 by combining all
 279 vertical mixing processes into a single term, expressing the rates of diapycnal mixing and
 280 advection with a single coefficient, κ . We excluded entrainment from the simplified budget
 281 because temporal variability in MLD (i.e. $dMLD/dt$) cannot be estimated readily from ship-based
 282 sampling. The simplified budget is represented by:

$$283 \quad \text{MLD} \cdot \frac{dC}{dt} = F_d + F_C + F_P + \frac{C_{\text{deep}} - C}{dz} \kappa \quad (3)$$

284 where F_d , F_C and F_P are the diffusive, small bubble and large bubble air-sea exchange fluxes, as
 285 described above. We evaluated this budget for Ar and N_2 over one mixed layer O_2 re-
 286 equilibration timescale, τ_{O_2} (defined in section 3.1.2, Eq. 6, and derived in section S1 of the SI),
 287 prior to each calculation derived from the full model simulations. As in the full simulations, we
 288 set the starting gas concentrations to equilibrium values (i.e. $C(t-\tau_{O_2}) = C_{\text{eq}} \frac{SLP}{1 \text{ atm}}$) and performed
 289 calculations in 0.25-day increments. The same environmental data used to force the full model
 290 simulations (i.e. u_{10} , SST and SLP) were applied in Eq. 3. Finally, we obtained $\Delta N_2'$ by
 291 subtracting the derived difference between ΔAr and ΔN_2 ($\Delta N_2^{\text{est}} - \Delta Ar^{\text{est}}$) from the
 292 corresponding ΔN_2 value predicted by the full model (ΔN_2^{true})

$$293 \quad \Delta N_2' = \Delta N_2^{\text{true}} - (\Delta N_2^{\text{est}} - \Delta Ar^{\text{est}}) \quad (4)$$

294 and recalculated $\Delta O_2/N_2'$ from $\Delta N_2'$ following Eq. 1.

295 In field studies, ΔN_2^{true} will be the measured value, and ΔN_2^{est} and ΔAr^{est} will be values
 296 predicted by the simplified gas budget (Eq. 3) using environmental data over one τ_{O_2} before
 297 observations. An example of the approach is presented in the SI (Fig. S2). Whereas estimates of
 298 u_{10} , SST and SLP over τ_{O_2} can be obtained from readily available reanalysis products, the time-
 299 histories of MLD, surface salinity, and sub-surface conditions are more difficult to estimate. For
 300 compatibility with field studies, we therefore fixed these terms (MLD, salinity, deep temperature,
 301 deep salinity, κ , $\Delta N_2/Ar_{\text{deep}}$) over τ_{O_2} at values corresponding with the time of ΔN_2^{true} (i.e. the
 302 time of in-situ sampling during field sampling). Moreover, given the paucity of in-situ
 303 subsurface noble gas measurements, we set ΔAr_{deep} to 0 % in all N_2' calculations, and held
 304 $\Delta N_2/Ar_{\text{deep}}$ constant at values from the full model run corresponding with the time of ΔN_2^{true} . In
 305 section 3.4.3, we evaluate errors in $\Delta N_2'$ and $\Delta O_2/N_2'$ resulting from these simplifying
 306 assumptions.

307

308 **3 Results and Discussion**

309 Differences between mixed layer $\Delta O_2/Ar$ and $\Delta O_2/N_2$ are most simply represented using
 310 the term $\Delta N_2/Ar$ (i.e. $([N_2/Ar]/[N_2/Ar]_{\text{eq}} - 1) \cdot 100 \%$), which is not sensitive to ΔO_2 , and thus not
 311 dependent on biological O_2 production in our modeling framework (Figs. S3, S6). Our
 312 experimental simulations (Ex-IF and Ex-IC; section 3.1) were designed to evaluate the effects of
 313 different physical factors on $\Delta N_2/Ar$, including bubble-mediated and diffusive gas transfer,
 314 vertical mixing and sea ice cover. The realistic simulations (real-OSP and real-BB; section 3.2)
 315 allowed us to evaluate the combined influence of these processes, and test our N_2' framework
 316 under typical oceanographic conditions. Below, we discuss the relative effects of different
 317 processes on gas variability, present a validation of the model against field observations, and
 318 show that our N_2' approach can correct for most of the difference between ΔN_2 and ΔAr
 319 saturation. We conclude by evaluating $\Delta O_2/N_2'$ as an NCP tracer and identifying the main
 320 sources of uncertainty associated with the use of this approach. In a subsequent paper, we will
 321 present a field validation of $\Delta O_2/N_2'$ measurements for NCP derivation. The SI of the present
 322 manuscript contains details and annotated software scripts for applying the N_2' approach to field
 323 data (section S3).

324

325 3.1 Mixed layer model experimental simulation results

326 A quasi-steady-state condition can be predicted from the MLD budget described in Eq. 3.
 327 Analysis of these conditions in our model reveals that bubble processes, mediated by sustained
 328 high wind speeds, can induce the largest $\Delta N_2/Ar$ disequilibria, with values potentially exceeding
 329 1.5 % at u_{10} of 20 $m s^{-1}$ (Fig. 1). Notably, elevated wind speeds always produce positive $\Delta N_2/Ar$
 330 (i.e. $\Delta N_2 > \Delta Ar$ and $\Delta O_2/Ar > \Delta O_2/N_2$), because of the lower solubility of N_2 relative to Ar (Fig.
 331 S), and its greater sensitivity to small bubble injection (Hamme et al., 2019; Liang et al., 2013).
 332 However, the bubble effect can be either dampened or enhanced by vertical mixing processes,
 333 such that the quasi-steady-state value of $\Delta N_2/Ar$ represents the relative influence of bubble
 334 processes and sustained mixing, which may increase or decrease $\Delta N_2/Ar$, depending on
 335 $\Delta N_2/Ar_{deep}$. The role of these two processes is reflected in the equation for the quasi-steady-state
 336 gas concentration, C_{SS} , derived in section S1 of the SI from the analytical solution to the N_2 '
 337 MLD gas budget (Eq. 3):

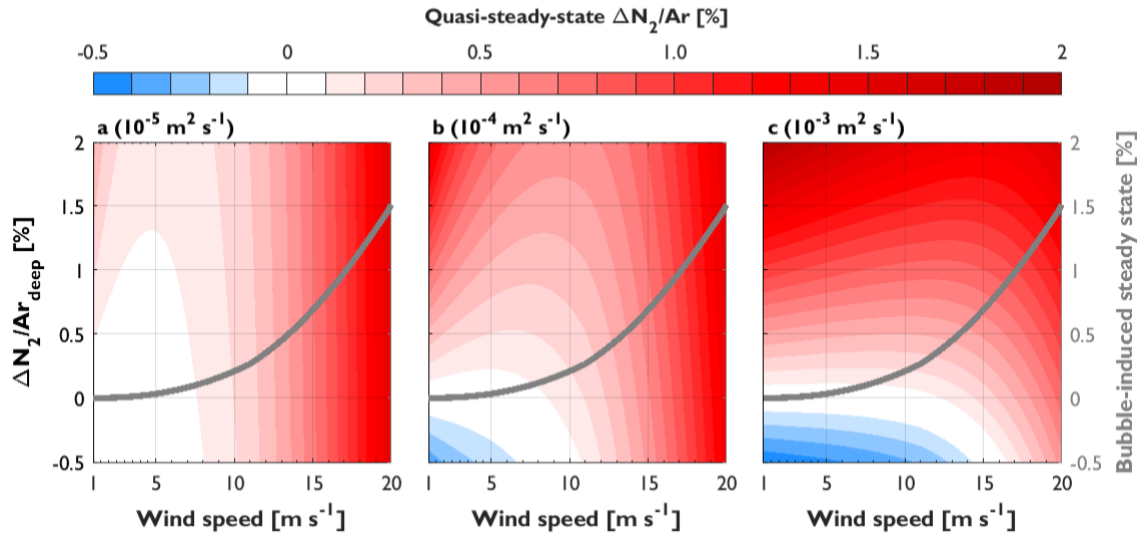
$$338 \quad C_{SS} = \frac{k_T C_{eq} (1 + \Delta_{eq}) \frac{SLP}{1 atm} + \frac{\kappa}{dz} C_{deep}}{k_T + \frac{\kappa}{dz}}. \quad (5)$$

339 Here, k_T is the combined u_{10} -dependent diffusive and bubble-mediated exchange velocity, and
 340 Δ_{eq} is the bubble-induced steady-state supersaturation anomaly. Evaluating Eq. 5 for Ar and N_2
 341 enables derivation of the quasi-steady-state $\Delta N_2/Ar$ value.

342 As shown in Fig. 1, surface $\Delta N_2/Ar$ depends, to first order, on u_{10} , vertical mixing rates
 343 and the value of $\Delta N_2/Ar$ below the mixed layer. As rates of vertical mixing increase and/or
 344 $\Delta N_2/Ar_{deep}$ decreases, bubble effects are dampened. For example, for κ and $\Delta N_2/Ar_{deep}$ values of
 345 $10^{-3} m^2 s^{-1}$ and -0.5 %, respectively, our model predicts negative quasi-steady-state $\Delta N_2/Ar$
 346 across a range of wind speeds ($u_{10} < 15 m s^{-1}$). Without vertical mixing, $\Delta N_2/Ar$ is set by the
 347 relative bubble-induced supersaturation states, Δ_{eq} , of N_2 and Ar (grey lines in Fig. 1), while in
 348 the absence of bubble processes, the quasi-steady-state $\Delta N_2/Ar$ falls between $\Delta N_2/Ar_{deep}$ and
 349 zero, depending on the strength of mixing (evaluate Eq. 5 for Δ_{eq} set to 0 %). This analysis
 350 illustrates the importance of bubble processes and vertical mixing in setting baseline $\Delta N_2/Ar$ in
 351 marine surface waters.

352 As described below, variability in u_{10} , SST and mixing strength on shorter time-scales
 353 (i.e. days) can induce significant transient signals in $\Delta N_2/Ar$. In contrast, atmospheric pressure
 354 alters all gas saturation states equally, such that SLP variability has no effect on $\Delta N_2/Ar$ (Hamme
 355 et al., 2019).

356
 357



358
 359 **Figure 1.** The combined effects of wind speed and mixing on steady-state $\Delta N_2/Ar$ derived from
 360 model simulations. Colour scaling represents the quasi-steady-state surface $\Delta N_2/Ar$ predicted by
 361 our model at SST and salinity values of 10 °C, and 34 PSU, respectively, based on equations
 362 presented in section S1.2 of the SI. The thick grey line represents the average bubble-induced
 363 steady-state condition (i.e. proportional to $\Delta_{eq,N_2}/\Delta_{eq,Ar}$) without mixing over a range of SST (0-
 364 25 °C). Panels represent a gradient from weakest (a) to strongest (c) mixing, with values of the
 365 mixing coefficient, κ , given at the top left of each panel.

366

367 3.1.1 Effects of variable wind speed, temperature and sea ice coverage

368 In practice, the ocean mixed layer rarely exists in a steady-state condition, and it is thus
 369 necessary to understand the dynamic response of mixed layer gases to transient physical
 370 perturbations. We used our experimental simulations to examine the response of $\Delta N_2/Ar$ to rapid
 371 changes in u_{10} (Ex-IF 1, 3, 4), SST (ΔSST ; Ex-IF 2, 3, 4) and sea ice cover (Ex-IC 1). In these
 372 simulations, u_{10} variability induces large responses in surface $\Delta N_2/Ar$ resulting from bubble
 373 processes, with the rate of re-equilibration to steady-state values also depending on u_{10} (Fig. 2a,
 374 c). In our simulations without mixing or rapid SST changes (Ex-IF 1a; Fig. 2a), the maximum
 375 $\Delta N_2/Ar$, was $\sim 0.7\%$ at a wind speed of 15 m s^{-1} , but values can exceed 1.5% for speeds $>20\text{ m}$
 376 s^{-1} (Fig. 1).

377 Temperature changes can enhance or dampen $\Delta N_2/Ar$ disequilibria by affecting gas
 378 saturation states over both long (i.e. seasonal) and shorter (days to weeks) time-scales (e.g.
 379 Emerson & Stump, 2010; Hamme et al., 2019; Hamme & Emerson, 2002; Hamme &
 380 Severinghaus, 2007; Steiner et al., 2007). If air-sea exchange rates are low, temperature-driven
 381 $\Delta N_2/Ar$ disequilibrium can persist for extended periods, while rapid ΔSST or periodic elevated
 382 wind events induce near-instantaneous disturbances in $\Delta N_2/Ar$, preventing gases from reaching
 383 steady-state values. In the absence of mixing, gas supersaturation anomalies will increase
 384 (decrease) if the rate of warming (cooling) exceeds the rate of re-equilibration via air-sea
 385 exchange. While bubble processes only produce positive $\Delta N_2/Ar$, temperature changes can lead
 386 to negative $\Delta N_2/Ar$ (i.e. $\Delta O_2/Ar < \Delta O_2/N_2$). Such SST effects occur through two mechanisms,
 387 which are represented in the Ex-IF 2 and Ex-IF 3 simulations (Fig. 2b, c). The first is a transient

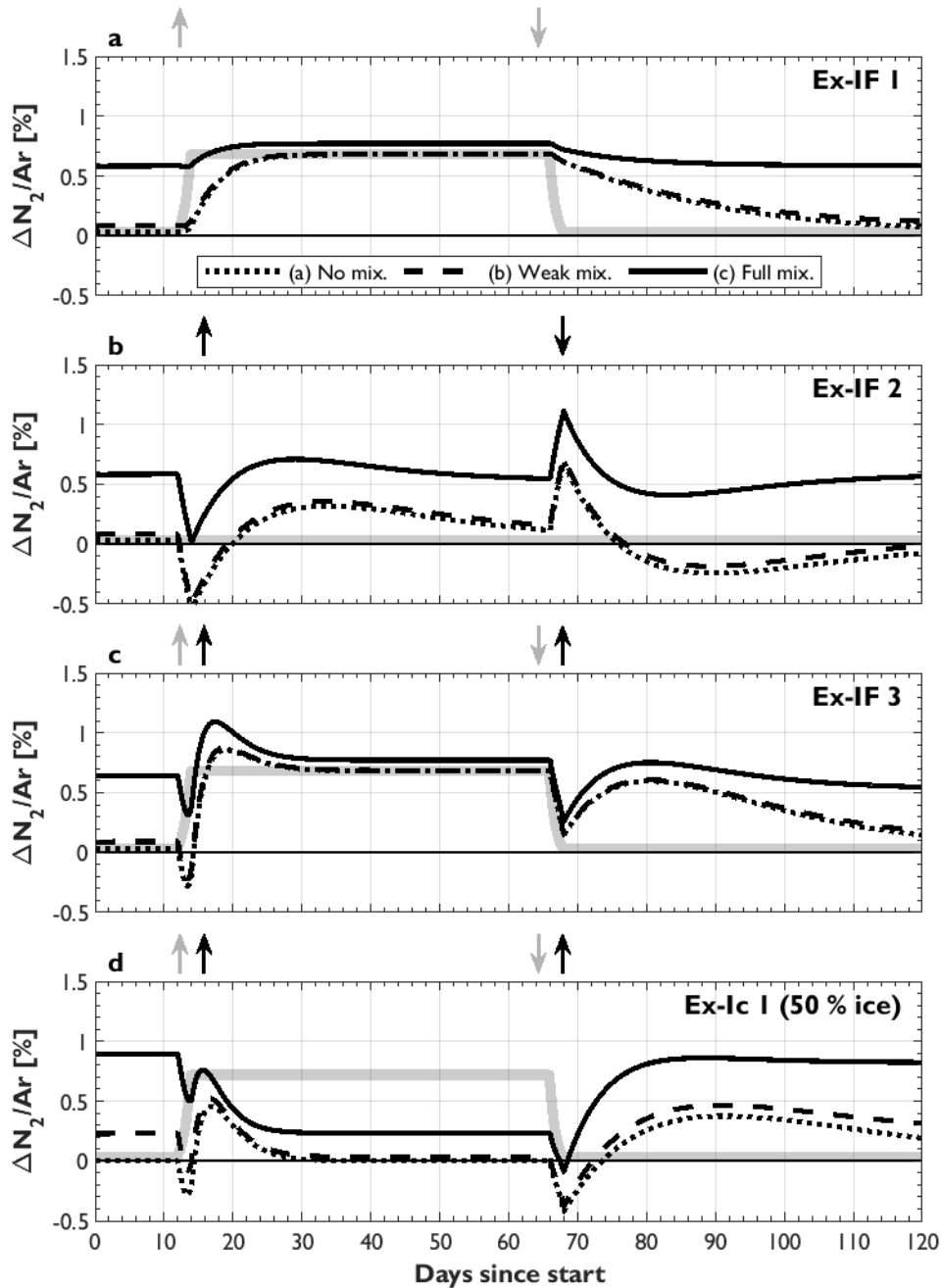
388 response to rapid warming (day 12), which causes ΔAr to increase more than ΔN_2 as a result of
389 the greater SST-dependent solubility of Ar (Fig. S1a). Subsequently, as SST stabilizes, and/or
390 ventilation rates increase, the sign of $\Delta\text{N}_2/\text{Ar}$ reverses (i.e. $\Delta\text{N}_2 > \Delta\text{Ar}$; days 20-65), as Ar re-
391 equilibrates more rapidly via diffusive air-sea exchange (Fig. S1c). Conversely, $\Delta\text{N}_2/\text{Ar}$ can
392 increase transiently following rapid cooling (Fig. 2b, days 65-68), before air-sea exchange
393 effects dominate once again to produce values lower than steady-state conditions. This response is
394 attributable to the greater cooling-induced increase in Ar solubility, followed by faster Ar re-
395 equilibration (Fig. 2b, >day 68), resulting in $\Delta\text{Ar} > \Delta\text{N}_2$ and potentially negative $\Delta\text{N}_2/\text{Ar}$.

396 Temperature effects can persist for long time-periods if air-sea exchange is weak (Fig.
397 2b-d; >day 75) or if SST continues to change steadily. Notably, rapid warming (cooling) will not
398 always produce transiently negative (positive) $\Delta\text{N}_2/\text{Ar}$, as the resulting gas perturbation depends
399 on the magnitude of ΔSST , prior gas conditions, and other gas fluxes (e.g. vertical mixing;
400 section 3.1.2). For example, during the second warming event in Ex-IF3 (Fig. 2c, day 65)
401 $\Delta\text{N}_2/\text{Ar}$ remains positive, but decreases, since prior values were near the u_{10} -dependent quasi-
402 steady-state condition. This scenario may be more likely in real conditions, as $\Delta\text{N}_2/\text{Ar}$ is often
403 positive in oceanic surface waters (see section 3.2 below).

404 In simulations conducted with partial ice cover (50 %; Ex-IC), the presence of ice
405 dampened u_{10} effects and accentuated SST controls on gas saturation states (Fig. 2d). The effects
406 of ΔSST persisted for significantly longer in ice-covered conditions due to reduced ventilation
407 rates. Moreover, gases approached 100 % saturation, rather than the bubble-induced
408 supersaturation states (grey line in Fig. 2d). The exact response depends on the gas exchange
409 model employed and the fraction of ice cover but a sensitivity analysis with different gas
410 exchange parameterizations (Butterworth & Miller, 2016; Islam et al., 2016; Loose et al., 2014)
411 produced the same general results, albeit with slightly variable re-equilibration times (not
412 shown). Our results thus reproduce the expected effects of sea ice dampening of gas exchange,
413 and the persistence of gas disequilibria caused by other physical factors (DeGrandpre et al.,
414 2020; Manning et al., 2017). The suppression of bubble effects under ice-covered conditions
415 (Nilsson et al., 2001) reflects the reduction in sea states and wave breaking activity (Liang et al.,
416 2017; Voermans et al., 2019; Woolf & Thorpe, 1991). Under partial or full ice-cover, other
417 physical processes are therefore more significant in generating mixed layer $\Delta\text{N}_2/\text{Ar}$ disequilibria
418 (see section 3.2). These results demonstrate the potential impact of sea ice dynamics in driving
419 O_2 , Ar and N_2 saturation anomalies. Future work should characterize the contributions of ice
420 formation or melt to $\Delta\text{O}_2/\text{Ar}$ and $\Delta\text{O}_2/\text{N}_2$ deviations.

421

422



423

424 **Figure 2.** Results from model simulations showing derived $\Delta N_2/Ar$ under different experimental
 425 perturbations. The three black lines in each panel represent the different mixing scenarios
 426 (described in panel a), and the thick light grey lines depict expected steady-state $\Delta N_2/Ar$ values
 427 resulting from bubble-induced supersaturation in each model run (grey lines in Fig. 1). Arrows
 428 above the panels represent step changes of increasing (up arrow) or decreasing (down arrow)
 429 wind speed (light grey) and SST (black). Details of imposed experimental conditions are
 430 presented in Table 1. The first three panels present simulations for ice-free conditions, while the
 431 bottom panel presents results with simulations containing 50% ice cover.

432

433 3.1.2 The role of vertical mixing

434 The results from our simulations excluding vertical mixing (run a) are consistent with
 435 Hamme & Emerson (2002) who demonstrate the first-order control of temperature changes and
 436 bubble-mediated gas exchange in controlling surface inert gas conditions. However, our
 437 simulations including mixing processes (runs b, c) highlight the key role of mixing in altering
 438 surface $\Delta N_2/Ar$. For example, vertical mixing of water parcels with different temperatures can
 439 induce supersaturation in O_2 , Ar and N_2 due to the non-linear temperature-dependence of gas
 440 solubility (Fig. S1; Hamme et al., 2019; Ito & Deutsch, 2006). Since temperature effects on O_2
 441 and Ar are nearly identical, surface $\Delta O_2/Ar$ will be largely insensitive to mixing if subsurface gas
 442 anomalies are negligible (i.e. subsurface $\Delta O_2/Ar$ near 0 %). However, throughout most of the
 443 ocean, waters below the mixed layer are depleted in O_2 so that surface $\Delta O_2/Ar$ and $\Delta O_2/N_2$ will
 444 be negatively biased in regions of active vertical mixing (see below; Izett et al., 2018; Teeter et
 445 al., 2018). Moreover, decoupling between surface $\Delta O_2/Ar$ and $\Delta O_2/N_2$ will occur through mixing
 446 of water masses with differing temperatures (or salinities, to a lesser-degree) as a result of the
 447 lower temperature-sensitivity of N_2 solubility (Fig. S1a), or from mixing of water parcels with
 448 subsurface $\Delta N_2/Ar$ not equal to 0 % (as observed throughout most of the ocean; Shigemitsu et
 449 al., 2016).

450 These mixing effects are represented in our model simulations, where weak vertical
 451 fluxes (run b; dashed lines in Fig. 2) lead to only minor deviations in surface $\Delta N_2/Ar$ from the
 452 bubble-induced value (compare dotted, dashed and grey lines in Fig. 2). Conversely, higher
 453 mixing fluxes (run c) may result in significantly elevated $\Delta N_2/Ar$. As predicted by our quasi-
 454 steady-state analyses (Fig. 1), surface $\Delta N_2/Ar$ in simulations including mixing is weighted
 455 between end members represented by the bubble-induced supersaturation ratio of N_2 and Ar, and
 456 $\Delta N_2/Ar_{deep}$. The resulting mixed layer value depends on the relative influence of air-sea exchange
 457 (i.e. k_T) and vertical mixing (κ/dZ). At low wind speeds or high mixing rates, surface $\Delta N_2/Ar$ is
 458 closer to $\Delta N_2/Ar_{deep}$ (Fig. 2; days <12 and >68) and potential deviations from the bubble-induced
 459 steady-state value can exceed ~2 % (Fig. 1c). In contrast, at higher u_{10} (Fig. 2a, c; days ~12-65)
 460 or low κ , air-sea exchange fluxes drive surface $\Delta N_2/Ar$ towards the bubble-induced
 461 supersaturation value, thus minimizing the effect of mixing fluxes.

462 While mixing can produce large $\Delta N_2/Ar$ anomalies, the results from Ex-IF 2-4
 463 demonstrate that the effects of rapid ΔSST and sea ice coverage are similar, regardless of the
 464 mixing scenario. Specifically, mixing shifts the baseline in $\Delta N_2/Ar$, but the transient responses to
 465 ΔSST in Ex-IF 2 are similar in all mixing scenarios. Similarly, as sea ice dampens the wind
 466 effect, strong mixing caused surface $\Delta N_2/Ar$ to approach $\Delta N_2/Ar_{deep}$ rather than the bubble-
 467 induced supersaturation state.

468 Throughout most of the ocean, the rate of air-sea exchange will typically exceed turnover
 469 via mixing ($k_T > 3.3 \text{ m d}^{-1}$ at wind speeds $> 7 \text{ m s}^{-1}$ and canonical κ_Z , $10^{-4} \text{ m}^2 \text{ s}^{-1}$; Cronin et al.,
 470 2015; Whalen et al., 2012). This implies that mixing can cause baseline shifts in surface $\Delta N_2/Ar$
 471 (Figs. 1-4), but that elevated wind events should still dominate on short time-scales, as observed
 472 in our experimental simulations (Ex-IF 1,3 and Ex-IC). Nonetheless, vertical mixing remains
 473 important in decreasing the re-equilibration timescale of mixed layer gas anomalies. When κ is
 474 high, gas residence times are reduced, more rapidly erasing any potential bubble-induced
 475 supersaturation effects. The analytical solution to our simplified MLD budget is useful for

476 diagnosing this effect as κ appears in the exponential term of the solution (Eq. 5), and therefore
 477 influences the rate constant of gas re-equilibration. Our definition of τ_{O_2} (Eq. 6), the O_2 re-
 478 equilibration time-scale over which N_2 ' calculations are performed (see sections 2.2, 3.4.1 and S1
 479 in the SI), also includes the mixing coefficient κ .

$$480 \quad \tau_{O_2} = \frac{-\ln(0.01) \cdot \text{MLD}}{\left(k_T + \frac{\kappa}{dz}\right)} \quad (6)$$

481

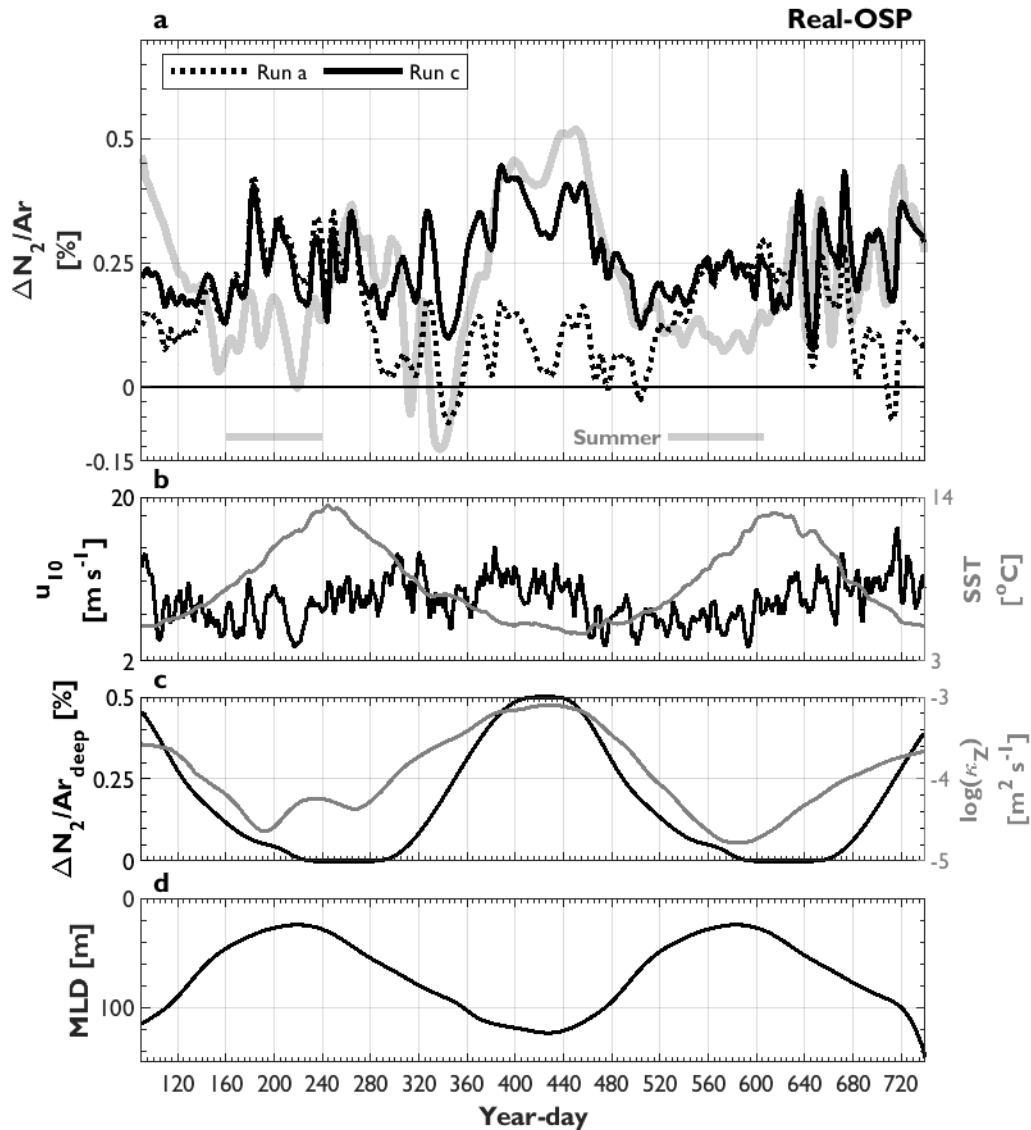
482 3.2 Realistic simulations

483 The main processes driving variability in $\Delta N_2/\text{Ar}$ in our experimental runs are also
 484 apparent in the realistic simulations (real-OSP in Fig. 3, and real-BB in Fig. 4). Under the more
 485 realistic scenarios, however, SST and differential gas exchange rates exerted the strongest
 486 controls on $\Delta N_2/\text{Ar}$ over long time-scales. Indeed, in both the real-OSP and real-BB simulations,
 487 ΔAr and ΔN_2 followed seasonal changes in SST, with transient modifications during periods of
 488 elevated wind-speeds (Figs. S4, S5). The OSP and Baffin Bay runs without mixing generally
 489 resemble the results of experiment Ex-IF 2a (ΔSST at constant u_{10}). The elevated spring and
 490 summertime $\Delta N_2/\text{Ar}$ in both sets of runs (days ~ 155 -255 and ~ 520 -620 in real-OSP, Fig 3; and
 491 days ~ 190 -230 in real-BB, Fig. 4) is consistent with increased gas supersaturation states, and the
 492 slower re-equilibration rate of N_2 over Ar following positive ΔSST . In the real-OSP run without
 493 mixing (run a), a net warming of $\sim 9^\circ \text{C}$ during the spring and summer caused $\Delta N_2/\text{Ar}$ to increase
 494 to $\sim 0.4\%$ (corresponding with ΔN_2 and ΔAr increases to $\sim 3\%$; Figs. S4, S5). In real-BBa, the
 495 equivalent ΔSST raised $\Delta N_2/\text{Ar}$ to $\sim 0.8\%$ (ΔN_2 and ΔAr increase to $\sim 11\%$; Fig. S5). These
 496 positive $\Delta N_2/\text{Ar}$ values, which exceed the quasi-steady-state conditions (thick grey lines in Figs.
 497 3, 4), thus reflect seasonal warming. During conditions of elevated u_{10} and net cooling (days
 498 ~ 260 -400 and $> \sim 620$ in real-OSP and $>$ day 250 in real-BB), the decline in $\Delta N_2/\text{Ar}$ is again more
 499 consistent with temperature-dependent solubility effects, with short-term modifications by
 500 bubble processes. In these realistic scenarios, the decline in $\Delta N_2/\text{Ar}$ during cooling periods
 501 resembled the response in Ex-IF 2 (i.e. decreased $\Delta N_2/\text{Ar}$; Fig. 2b, c).

502 As observed in the experimental runs, the real-OSP and real-BB simulations also
 503 demonstrated a mixing effect on gas conditions, with vertical fluxes elevating surface gas
 504 anomalies, particularly during autumn and winter periods. The mixing effect on $\Delta N_2/\text{Ar}$ was
 505 most significant at higher κ , during MLD deepening (Figs. 3c, 4c), or under sea ice cover (Fig.
 506 4b), when $\Delta N_2/\text{Ar}$ approached $\Delta N_2/\text{Ar}_{\text{deep}}$. In the full mixing runs of both realistic simulations,
 507 $\Delta N_2/\text{Ar}$ was almost always higher than in the non-mixing runs. Exceptions occurred during
 508 periods of reduced summertime mixing in real-OSP (annotated in Fig. 3) when $\Delta N_2/\text{Ar}$ was
 509 equivalent in both mixing scenarios (and in all sensitivity model runs; see section 3.3), and
 510 between days 220 and 240 in real-BB, when mixing dampened the warming effect. Ultimately,
 511 seasonal variability in the mixing response will be sensitive to intra-annual variability in u_{10} ,
 512 $\Delta N_2/\text{Ar}_{\text{deep}}$ and κz , which we attempted to capture in our real-OSP simulations (Table 1).

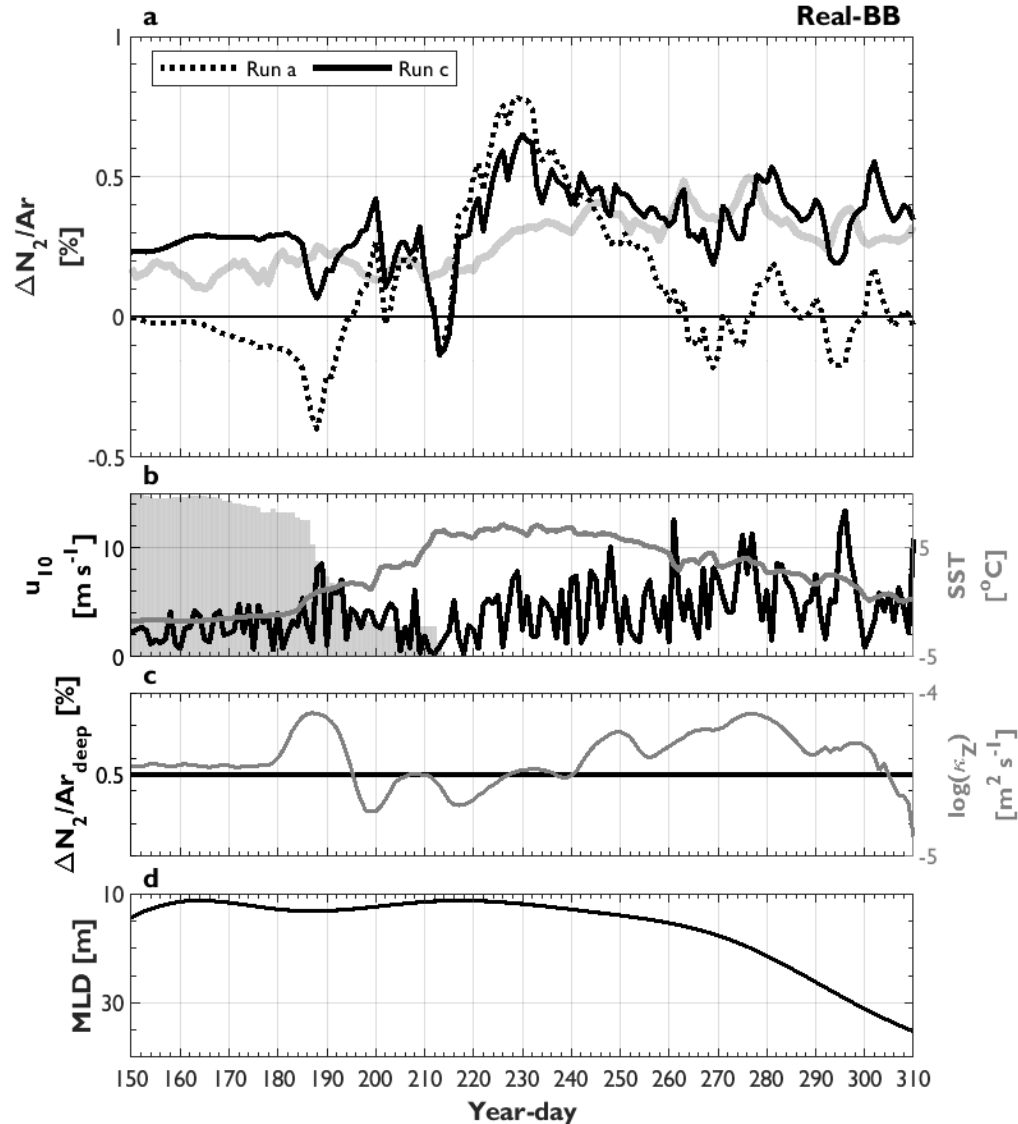
513 In contrast to the experimental runs, $\Delta N_2/\text{Ar}$ in the realistic simulations seldom achieved
 514 the quasi-steady-state condition (grey lines in Figs. 3, 4 predicted by Eq. 5). This reflects the
 515 high variability in environmental forcing, and the fact that thermal disequilibrium can persist for
 516 long periods (up to 60 days in our experimental simulations) under low wind speeds. This result
 517 demonstrates the simultaneous effects of various fluxes on gas saturation states. Only under

518 conditions of significant ice cover and high mixing does $\Delta N_2/Ar$ remain near to the steady state
 519 values.



520

521 **Figure 3.** Results from realistic model simulations of OSP in the Subarctic Northeast Pacific.
 522 Panel (a) shows $\Delta N_2/Ar$ in runs without (run a; dotted lines) and with (run c; solid lines) mixing,
 523 while panels (b)-(d) represent the forcing environmental data (details in Table 1). The x-axes
 524 represent the 2011 year-day (Jan. 2011 – Jan. 2013). The thick grey line in (a) depicts the quasi-
 525 steady-state condition (Eq. 5; Fig. 1) corresponding with run c. The grey bars in (a) (labelled
 526 “summer”) represent periods of weak mixing between June and September, and correspond with
 527 data shown in Fig. 6.



528

529 **Figure 4.** Results from realistic model simulations of Baffin Bay in the eastern Arctic. The x-
 530 axes represent the 2019 year-day (May – Oct.). The grey shading in (b) represents the ice-
 531 coverage as a percent of the figure y-scale. Refer to Fig. 3 caption and Table 1 for details.

532

533

3.3 Model validation and sensitivity tests

534

To validate our modelling approach in support of the subsequent N_2' analysis (section
 535 3.4.1), we compared N_2 and O_2 from our real-OSP run c simulation against a two-year cycle of
 536 surface measurements from the NOAA PMEL OSP mooring (provided by S. Emerson at
 537 https://www.nodc.noaa.gov/ocads/oceans/Moorings/Papa_145W_50N.html; Emerson et al.,
 538 2017). As shown in Fig. 5a, b, our model calculations forced with relevant environmental data
 539 and time-variable mixing terms agree well with the mooring gas data. The model is able to
 540 reproduce both short-term (associated with wind events) and long-term (associated with seasonal

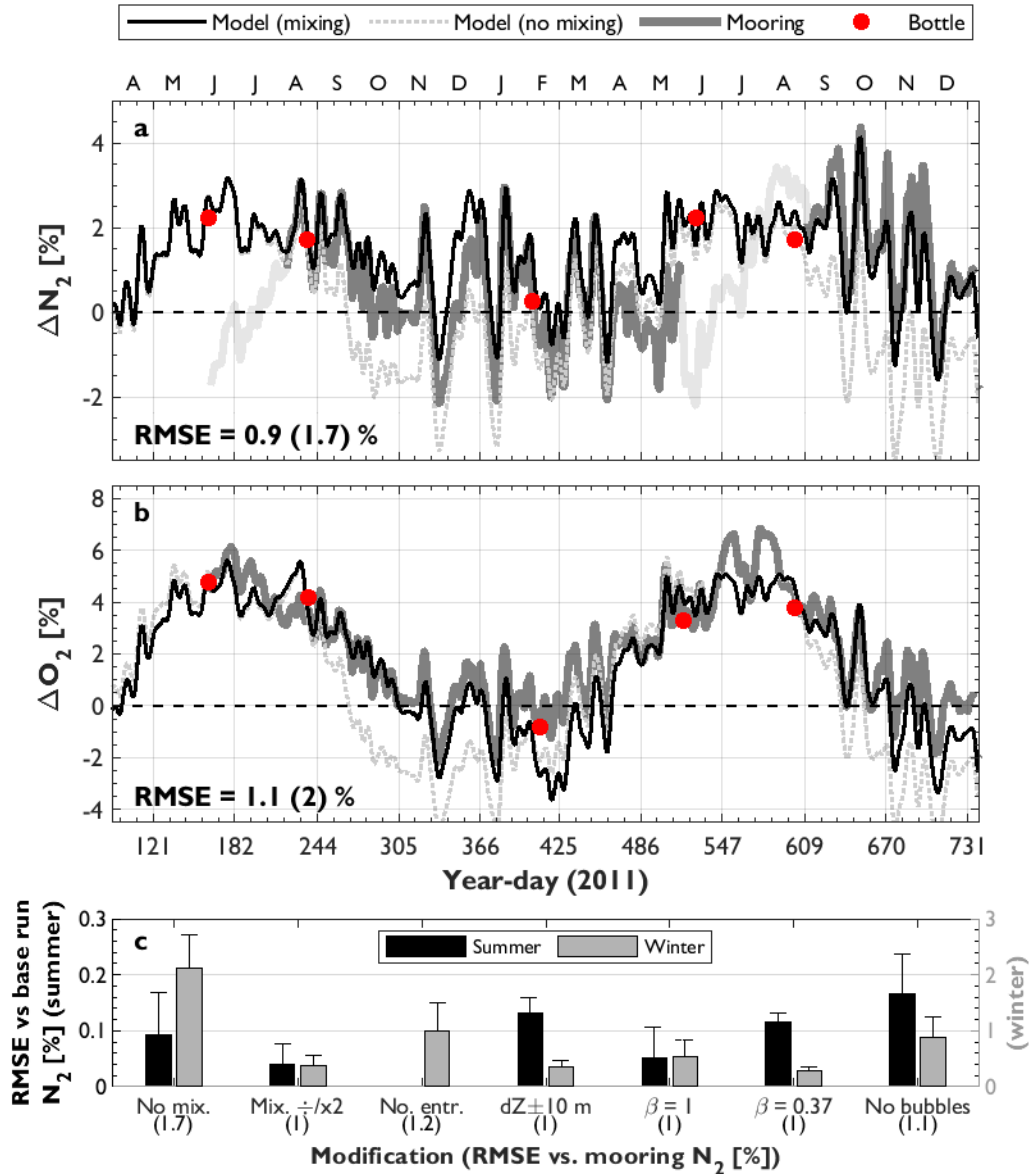
541 SST and mixing variability) responses of N_2 to environmental drivers, with an overall root mean
542 square error (RMSE) between the model and data of 1.0 % (range of offset between modeled and
543 observed N_2 $\sim 0 - 2.4$ %). Moreover, our modelled O_2 , which was forced with a mean annual
544 NCP time-series and subsurface O_2 observations at OSP, recaptures the observed annual cycle
545 with equally-small deviation from the in-situ time-series (RMSE = 1 %; range 0 – 3.1 %).

546 Residual differences between the model and observations can be explained by several
547 factors, including the potential effects of lateral advection (Emerson & Stump, 2010), which are
548 neglected in our calculations, and the smoothed mixed layer and mixing forcing conditions
549 applied in our model runs. In addition, interpolation of sparse ΔAr_{deep} and $\Delta N_2/Ar_{deep}$
550 observations from discrete gas sampling at OSP (February, June and August data from Hamme
551 et al., 2019) may not fully represent subsurface conditions across the full seasonal cycle. Indeed,
552 the poorest alignment between model and observed ΔN_2 occurs during the fall and early winter
553 (e.g. days $\sim 260-390$), when no subsurface gas observations were available. Moreover, while we
554 applied κ_z values corresponding with the location and timing of our model setting (from Cronin
555 et al., 2015), it is also possible that uncertainty in the κ_z dataset may contribute to differences
556 between the model and observed gas data. Importantly, however, the model run with realistic
557 mixing fluxes was able to better replicate the full seasonal cycles of N_2 and O_2 than the
558 simulation run without mixing (light grey line in Fig. 5a,b). Indeed, the model run without
559 mixing often under-estimates ΔN_2 , demonstrating the importance of vertical mixing in supplying
560 relatively high- N_2 to surface waters.

561 We tested the model sensitivity to flux parameterizations by performing additional
562 simulations in which the mixing terms (κ_z , dZ , entrainment) and bubble scaling coefficient (β)
563 were modified from the real-OSP full mixing run (Fig. 5c). Overall, we find that the model skill
564 at reproducing observed N_2 at OSP is most sensitive to the exclusion of bubble processes and
565 vertical flux terms. This result is consistent with other studies (e.g., Emerson et al., 2019;
566 Emerson & Bushinsky, 2016; Hamme & Severinghaus, 2007), which noted that explicit bubble
567 flux terms are required to explain gas observations. Moreover, we find that the model sensitivity
568 is greater in the wintertime at OSP. This reflects the reduced significance of bubble fluxes and
569 vertical mixing during summer months, as a result of lower wind speeds and upper ocean
570 turbulence. The weak sensitivity of the model to parameterizations in the summer months is a
571 key result as it supports the application of the present approach during time-periods when NCP
572 and carbon export are typically elevated, and when in-situ sampling from research vessels is
573 most common. Indeed, results vary by less than 0.25 % across all modified simulations between
574 June and August, as compared with deviations exceeding 1 % in winter periods.

575 Based on the comparisons of modeled and observed N_2 , we believe that our model
576 captures the main drivers of N_2 saturation variability in oceanic surface waters, particularly
577 during biologically-productive summer months. Although the model cannot be equally-validated
578 for Ar due to a lack of observations, we expect that our conclusions apply to this gas as well.
579 This exercise should also be taken as a rough validation of the Liang et al. (2013) bubble-flux
580 parameterization, which was previously evaluated in the North Pacific by Emerson & Bushinsky
581 (2016) using a similar model as that employed here. Importantly, the strong agreement between
582 our model results and observations over a two-year cycle justifies the air-sea flux and mixing
583 parameterizations used in our model simulations, and provides confidence in the N_2 ' approach
584 described below.

585



586

587 **Figure 5.** A comparison of modeled (thin lines) and observed (thick grey line) N_2 (a) and O_2 (b)
 588 supersaturation anomalies over a two-year cycle at OSP in the Subarctic Northeast Pacific. The
 589 modelled gas results are from the full mixing (run c; black line) and no mixing (run a; light grey
 590 line) real-OSP simulations and correspond with results and forcing parameters presented in Fig.
 591 3 and Table 1. Gas observations were obtained from the NOAA PMEL mooring at OSP. The
 592 light, thick-grey section of the mooring N_2 time-series in (a) represents a section of the record
 593 where the N_2 data may be biased by sampling artifacts (S. Emerson personal communication,
 594 2020). All lines represent 1-day smoothed values. The red dots in (a) and (b) represent discrete
 595 observations. The N_2 data (a) are mean February, June and August N_2 values from Hamme et al.
 596 (2019), and O_2 data (b) are from Rosette sampling at the specified times. The RMSE values
 597 presented at the top-right represent differences between modelled and mooring values for real-
 598 OSP run c (run a value in brackets). Values on the x-axis correspond with 2011 year-day, and
 599 labels at the top represent month. Panel (c) represents a sensitivity analysis on our model

600 parameterizations where the real-OSP with full mixing simulation ($\beta = 0.5$ and $dZ = \text{MLD to}$
 601 thermocline depth) was modified as indicated by the labels on the x-axis. The model sensitivity
 602 was evaluated during summer (July-Aug.; left axis) and a winter (Nov.-Feb.; right axis)
 603 segments. The bars represent the mean difference between the base and modified runs during
 604 these segments, with error bars depicting the range of values. The numbers below the x-axis
 605 labels are the overall RMSE between each modified model run and the real mooring N_2 data
 606 from OSP. Note that the summer sensitivity results are represented by the left y-axis, which is a
 607 factor of 10 smaller than the scale on the left axis, representing the winter results.

608

609 3.4 NCP calculations from O_2 and N_2 measurements

610 Divergence between mixed layer $\Delta\text{O}_2/\text{Ar}$ and $\Delta\text{O}_2/\text{N}_2$ (non-zero $\Delta\text{N}_2/\text{Ar}$) can lead to
 611 significant uncertainty in NCP estimates calculated from O_2 and N_2 observations. For a realistic
 612 range of ΔO_2 and $\Delta\text{N}_2/\text{Ar}$ in the ocean, absolute differences between $\Delta\text{O}_2/\text{Ar}$ and $\Delta\text{O}_2/\text{N}_2$ may
 613 exceed 2 % (Fig. S6a), which is of the same magnitude as ΔO_2 observed in many low
 614 productivity ocean regions. Relative differences between NCP tracers can exceed 100 % for low
 615 ΔO_2 , and will likely be significant over a large range of ocean conditions (Fig. S6b). These
 616 biases will propagate as errors in NCP estimates derived from observations of the biological O_2
 617 saturation anomaly calculated following Kaiser et al., (2005):

$$618 \quad \text{NCP} = k_{\text{O}_2} \cdot \Delta\text{O}_2/\text{N}_2 \cdot [\text{O}_2]_{\text{eq}} \quad (7)$$

619 Over a realistic range of SST (0-30 °C), salinity (30-35 PSU) and u_{10} (2-10 m s^{-1}), a bias in
 620 $\Delta\text{O}_2/\text{N}_2$ of 0.3 % (the mean value of $\Delta\text{O}_2/\text{Ar} - \Delta\text{O}_2/\text{N}_2$ in our realistic simulations; Table S1)
 621 would introduce $\sim 6 \text{ mmol O}_2 \text{ m}^{-2} \text{ d}^{-1}$ error in NCP estimates, while a bias of 1.1 % (the upper
 622 range in our simulations) would contribute up to $\sim 19 \text{ mmol O}_2 \text{ m}^{-2} \text{ d}^{-1}$ uncertainty. These errors
 623 may be comparable to those resulting from diel O_2 variability (up to ~ 5 to $>100 \text{ mmol O}_2 \text{ m}^{-2} \text{ d}^{-1}$;
 624 Wang et al., 2020) and vertical mixing of subsurface O_2 -deplete waters (~ 0 -50 and 60-190
 625 $\text{mmol O}_2 \text{ m}^{-2} \text{ d}^{-1}$ in offshore and coastal waters, respectively; Izett et al., 2018), depending on the
 626 ocean region sampled. However, the differences between $\Delta\text{O}_2/\text{Ar}$ and $\Delta\text{O}_2/\text{N}_2$ in our realistic
 627 simulations are almost as large in magnitude as reported $\Delta\text{O}_2/\text{Ar}$ values in many offshore regions
 628 of all ocean basins, which are typically smaller than $\sim \pm 5$ -10 % (e.g. Eveleth et al., 2014, 2017;
 629 Giesbrecht et al., 2012; Hamme & Emerson, 2006; Izett et al., 2018; Juranek et al., 2019;
 630 Lockwood et al., 2012; Munro et al., 2013; Palevsky et al., 2016; Ulfso et al., 2014; Wang et
 631 al., 2020). Thus, biases in the quantification of the biological O_2 saturation anomaly could lead to
 632 erroneous interpretations of NCP estimates from $\Delta\text{O}_2/\text{N}_2$ measurements and, in some regions,
 633 false conclusions regarding the metabolic status of surface waters (i.e. implied net heterotrophy
 634 from negative $\Delta\text{O}_2/\text{N}_2$ versus autotrophy from positive $\Delta\text{O}_2/\text{Ar}$; represented by outlined region in
 635 Fig. S6). These limitations motivate the need to correct $\Delta\text{O}_2/\text{N}_2$ observations for excess physical
 636 N_2 saturation, particularly in offshore waters where other biases are smaller.

637 Fortunately, our analyses demonstrate that differences between $\Delta\text{O}_2/\text{Ar}$ and $\Delta\text{O}_2/\text{N}_2$
 638 respond systematically to differential physical gas fluxes and environmental perturbations,
 639 enabling us to apply appropriate corrections. We thus derived a new term, N_2' (calculations
 640 described in section 2.2 and software scripts provided at doi.org/10.5281/zenodo.4024952),
 641 which holds significant value as a tracer for physically-induced changes in the mixed layer O_2 .
 642 As we discuss below, $\Delta\text{O}_2/\text{N}_2'$, derived from Optode (O_2) and GTD (N_2) measurements and

643 calculations from a simplified MLD budget, provides a good analog for $\Delta O_2/Ar$ -based NCP
 644 estimates.

645

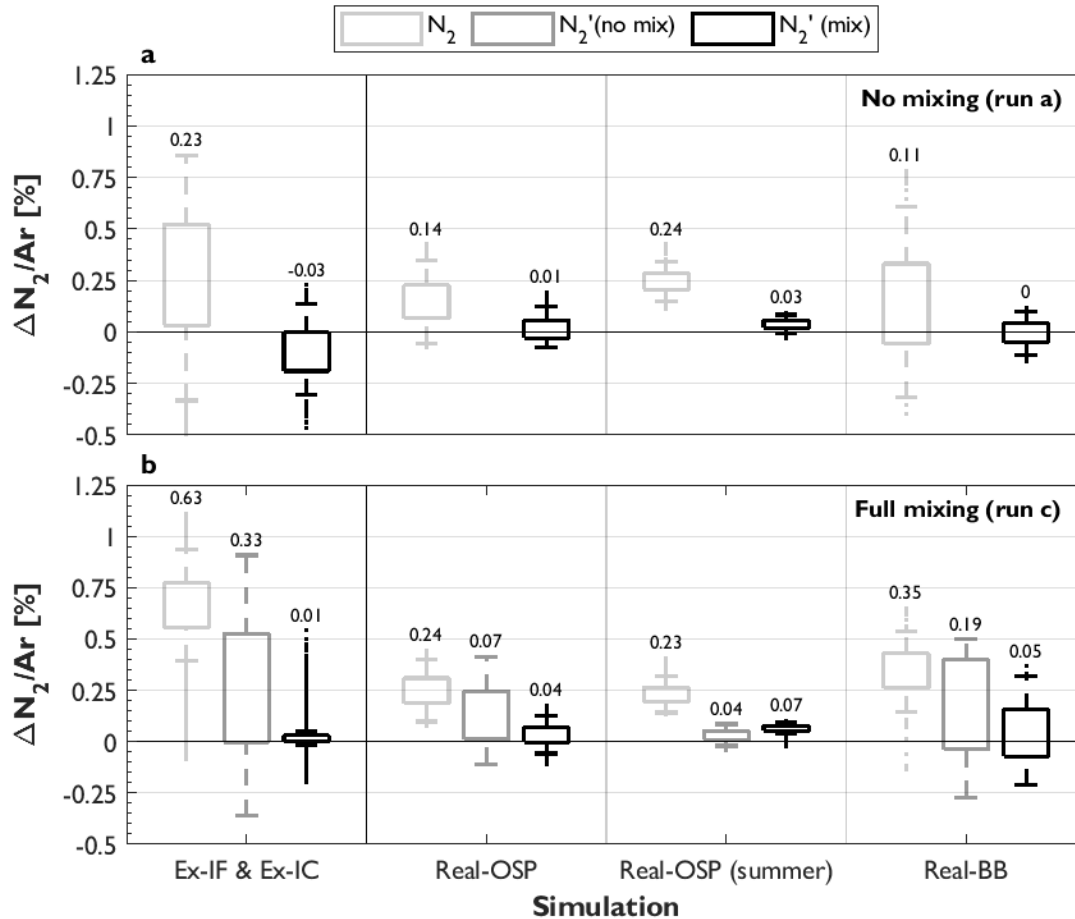
646 3.4.1. N_2' in mixed layer model setting

647 We tested the performance of our N_2' approach using the experimental and realistic
 648 simulations (Figs. 2-4). We treated the simulated gas values as “true” (i.e. analogous to in-situ
 649 ocean observations; see Eq. 4) and applied the N_2' approach based on readily-available data from
 650 reanalysis products or field observations. In deriving $\Delta N_2'$, we thus applied the same
 651 environmental forcing data (SST, u_{10} and SLP) as in the full model simulations, but assumed
 652 constant values backwards in time for MLD, surface salinity, κ , and $\Delta N_2/Ar_{deep}$, to mirror the
 653 information available from field studies (see below, section 3.4.3).

654 Overall, N_2' successfully corrects for differences in surface water ΔAr and ΔN_2 , thereby
 655 reducing biases between $\Delta O_2/Ar$ and $\Delta O_2/N_2$ (Fig. 6). Across all experimental simulations,
 656 median $\Delta N_2'/Ar$ was $\sim 0\%$ and ~ 0.01 in the runs without (a) and with (c) mixing, respectively. In
 657 comparison, uncorrected $\Delta N_2/Ar$ was significantly larger than 0, with median values of 0.23 and
 658 0.63 % (maximum 1.1 %). In the realistic simulations, median $\Delta N_2'/Ar$ and $\Delta O_2/Ar - \Delta O_2/N_2'$
 659 were ~ 0.01 (range -0.24 to 0.3 %; Fig. 6, Table S1), demonstrating that differences between
 660 $\Delta O_2/Ar$ and $\Delta O_2/N_2$ can be corrected using simple MLD budget computations performed over an
 661 estimated O_2 re-equilibration time (Eq. 6).

662 The remaining $\Delta N_2'/Ar$ disequilibria is attributable to the simplifying assumptions in the
 663 N_2' approach, which we discuss in section 3.4.3. We observed the largest remaining biases in
 664 $\Delta N_2'/Ar$ during the summer period of the real-BB full mixing simulation (Fig. S9b). These
 665 relatively large remaining offsets between $\Delta N_2'$ and ΔAr resulted from significant temporal
 666 variability in subsurface gas concentrations in the BB simulations, which cannot be represented
 667 in N_2' calculations (see sections 2.1.1, 3.4.3 and S2.2 for details). However, we believe that these
 668 biases represent the upper limit of values expected from application of the present approach to
 669 real data sets, as subsurface gas conditions are likely to vary less in reality than in our model.
 670 Additional remaining biases in $\Delta N_2'/Ar$ occurred during the autumn months of the real-OSP full
 671 mixing scenario when vertical entrainment was significant (\sim days 230-330 and >600 in Fig.
 672 S9a), and in early summer (\sim days 160-200 and ~ 525 -565) when the N_2' budget was unable to
 673 resolve the relatively strong mixing occurring prior to this time. Despite these offsets, N_2' is
 674 useful in reducing differences between $\Delta O_2/Ar$ and $\Delta O_2/N_2$ observations, and $\Delta N_2'/Ar$ was
 675 almost always lower than $\Delta N_2/Ar$ in all of our simulations.

676 Given the sparsity of oceanic mixing rate estimates (e.g. Whalen et al., 2012) or
 677 subsurface Ar and N_2 measurements (e.g. Hamme et al., 2019), it may be difficult to constrain
 678 the mixing flux terms in our N_2' model (see below, sections 3.4.2 and 3.4.3). We therefore
 679 performed an additional set of N_2' calculations to test our approach when vertical mixing fluxes
 680 are neglected. This term, which we denote as $\Delta N_2'(\text{no mix.})$, was derived by setting κ to $0 \text{ m}^2 \text{ s}^{-1}$
 681 in the N_2' calculations. We find that $\Delta N_2'(\text{no mix.})/Ar$ does not fully correct for differences
 682 between $\Delta O_2/Ar$ and $\Delta O_2/N_2$ in most simulations (Fig. 6). However, in a subset of real-OSP run
 683 c corresponding with mid-June to September (labelled bars in Fig. 3), $N_2'(\text{no mix.})$ successfully
 684 reduced $\Delta N_2'/Ar$ to a median value of $\sim 0.04\%$. This result is promising for in-situ applications in
 685 stratified ocean regions, when vertical mixing is small relative to other gas flux terms.



686

687 **Figure 6.** Distribution of $\Delta N_2/Ar$ and $\Delta N_2'/Ar$ in the experimental (left) and realistic (right)
 688 simulations runs without mixing (run a) and with mixing (run c) (details in Table 1). The
 689 numbers above each box represent the median $\Delta N_2/Ar$ or $\Delta N_2'/Ar$ values. A value of zero
 690 implies that N_2' provides a perfect analog for Ar. A subset of the OSP simulation is included to
 691 represent results in more stratified waters during summer months in the Subarctic Northeast
 692 Pacific (highlighted in Fig. 3a).

693

694

3.4.2 $\Delta O_2/N_2'$ as an in-situ NCP tracer

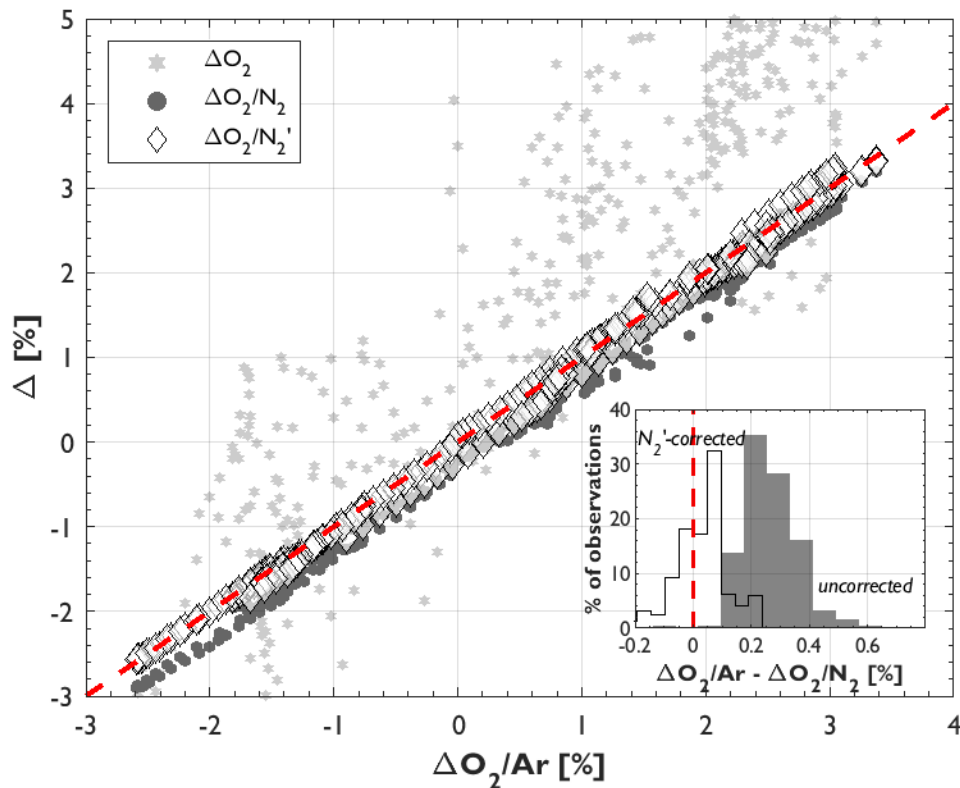
695

696 Our work demonstrates that $\Delta O_2/N_2'$ offers a robust analog for $\Delta O_2/Ar$ measurements.
 697 Indeed, we found that $\Delta O_2/N_2'$ performed significantly better than either ΔO_2 or uncorrected
 698 $\Delta O_2/N_2$ in reproducing $\Delta O_2/Ar$. As shown in Fig. 7, $\Delta O_2/N_2'$ was tightly correlated to $\Delta O_2/Ar$,
 699 with a linear regression slope that was not significantly different from unity, and an RMSE of
 700 0.03 %. This result suggests that NCP calculations based on $\Delta O_2/N_2'$ should be nearly-equivalent
 701 to $\Delta O_2/Ar$ -derived estimates, providing an alternative approach to isolate biological influences
 702 on mixed layer oxygen dynamics. Moreover, we have observed strong coherence between
 703 $\Delta O_2/Ar$ and $\Delta O_2/N_2'$ in observations obtained from underway ship-board surveys across broad
 spatial scales and hydrographic gradients (manuscript in preparation).

704 Field-based application of the N_2' approach will depend on proper characterization of
705 environmental histories and mixing environments. Quantification of the mixing terms, κ and
706 $\Delta N_2/Ar_{\text{deep}}$, will likely constitute the largest source of uncertainty in $\Delta O_2/N_2'$ (see section S2 of
707 the SI), as these values are generally poorly constrained by limited observations and strong
708 spatial or temporal variability. Recent work has provided several approaches to approximating κ
709 from direct or indirect estimates of turbulent dissipation rates (Chanona et al., 2018; Scheifele et
710 al., 2018; Whalen et al., 2012), and by proxy relationships with temperature and salinity (Cronin
711 et al., 2015), nitrous oxide (Izett et al., 2018) or inert gas measurements (Ito & Deutsch, 2006). It
712 is also possible to estimate $\Delta N_2/Ar_{\text{deep}}$ and κ from archived datasets (e.g. Hamme et al., 2019) or
713 circulation models (e.g. Castro de la Guardia et al., 2019; Shigemitsu et al., 2016). Moreover, as
714 demonstrated in Fig. 1, and in the simulations with weak or no mixing (Figs. 2, 3), vertical fluxes
715 have a relatively small impact on surface $\Delta N_2/Ar$ when mixing rates fall below $\sim 10^{-4} \text{ m}^2 \text{ s}^{-1}$, or
716 when $\Delta N_2/Ar_{\text{deep}}$ is less than $\sim 0.25\%$. Indeed, in our real-OSP and real-BB simulations forced
717 with time-variable and realistic κ_z and $\Delta N_2/Ar_{\text{deep}}$, surface $\Delta N_2/Ar$ converged on similar values
718 for both mixing scenarios between days during summer periods, when κ_z was small (Figs. 3, 4).
719 This suggests a negligible contribution of vertical fluxes to surface gas budgets during periods of
720 stratification, consistent with observations of reduced summertime vertical gas fluxes in mid-
721 latitude oceanic waters (e.g. Emerson & Stump, 2010; Izett et al., 2018; Pelland et al., 2018;
722 Plant et al., 2016). The implication of these results is that mixing terms can potentially be
723 neglected in N_2' corrections under conditions of moderate to strong stratification. Such
724 conditions occur over much of the ocean during periods of summer productivity.

725 In dynamic coastal waters where vertical mixing may contribute to a significant
726 divergence between $\Delta O_2/Ar$ and $\Delta O_2/N_2$, particularly in regions of subsurface or benthic
727 denitrification (see below, section 3.4.3), the resulting bias in NCP estimates may be small
728 compared with errors resulting from vertical mixing fluxes of O_2 and diel variability (section
729 3.4). Moreover, if ΔO_2 is elevated ($>5\%$) by strong biological production, relative differences
730 between $\Delta O_2/Ar$ and $\Delta O_2/N_2$ will remain smaller than the $\sim 20 - 40\%$ uncertainty in gas transfer
731 parameterizations (Fig. S6b; Bender et al., 2011; Wanninkhof, 2014). In offshore waters, where
732 ΔO_2 is typically nearer to equilibrium, and other biases in O_2 are small, N_2' corrections will be
733 necessary to minimize errors in NCP calculations. Overall, we conclude that underway $\Delta O_2/N_2$
734 measurements from Optode and GTD sampling, combined with careful application of the N_2'
735 calculations described here, can serve as an effective alternative to $\Delta O_2/Ar$ -based NCP sampling
736 across a wide range of oceanic conditions. This approach thus has the potential to significantly
737 increase the spatial and temporal coverage of marine NCP estimates.

738



739

740 **Figure 7.** The relationship between $\Delta\text{O}_2/\text{Ar}$ and ΔO_2 (light grey stars), $\Delta\text{O}_2/\text{N}_2$ (dark grey
 741 circles) and $\Delta\text{O}_2/\text{N}_2'$ (black/white diamonds) in the realistic model simulations (real-OSP and
 742 real-BB, simulations with full mixing only). The dashed red line shows the 1:1 fit. The inset
 743 shows the distribution of $\Delta\text{O}_2/\text{Ar} - \Delta\text{O}_2/\text{N}_2$ before (filled grey) and after (outlined) applying N_2'
 744 corrections.

745

746 3.4.3 Remaining biases and uncertainty in $\Delta\text{O}_2/\text{N}_2'$

747 Despite strong the coherence between $\Delta\text{O}_2/\text{N}_2'$ and $\Delta\text{O}_2/\text{Ar}$ (Fig. 7), and general
 748 agreement of ΔAr and $\Delta\text{N}_2'$ some biases remain. These are attributable to the simplifying
 749 assumptions in the N_2' calculations (i.e. constant MLD, salinity, κ and $\Delta\text{N}_2/\text{Ar}_{\text{deep}}$), made
 750 necessary by the limitation of field observations. The time-history of u_{10} , SST, and SLP prior to
 751 ship-board sampling in a given location can be obtained from remote sensing and reanalysis
 752 products, but estimates of MLD and salinity are most reliable from ship-board measurements.
 753 The subsurface and mixing terms (κ and $\Delta\text{N}_2/\text{Ar}_{\text{deep}}$) may be derived from measurements made at
 754 the time of underway gas sampling (see above), but will normally be obtained from external
 755 sources and assumed constant over τ_{O_2} . Across our realistic simulation runs, we found that the
 756 contribution of these simplifying assumptions to uncertainty in $\Delta\text{O}_2/\text{N}_2'$ was $\sim 0.07\%$ (Table S1;
 757 details in section S2 of the SI), which is small relative to other sources of error in NCP
 758 calculations, as discussed above. In general, these errors were largest during times of significant
 759 subsurface hydrographic and gas variability, as was the case in our real-BB simulation. While the
 760 settings in our BB runs may not be entirely representative of reality, and we were unable to
 761 validate the modeled time-series in this location, the N_2' results from these model runs should be

762 seen as upper limits of values expected from field studies. Errors associated with these
 763 assumptions can only be reduced by quantifying the time-variability of the relevant terms, which
 764 may be feasible from Argo floats near to cruise track observations, additional reanalysis products
 765 or numerical model output.

766 Additional uncertainty in field applications of the N_2' approach arises from the
 767 parameterization uncertainty in each of the terms (u_{10} , SST, SLP, F_d , F_C , F_P , β , MLD, κ and
 768 $\Delta N_2/Ar_{\text{deep}}$) used to predict $\Delta N_2/Ar$ (Eq. 3). To evaluate the magnitude of these errors, we
 769 performed a Monte Carlo analysis on the realistic simulations (real-OSP and real-BB, run c only)
 770 by randomly varying each of the input variables around their estimated parameter uncertainty
 771 (details in section S2 of the SI). We estimated a combined absolute parameterization error in
 772 $\Delta O_2/N_2'$ of 0.09 %, with the largest contributions coming from the SST product (Table S1). This
 773 is unsurprising given the seasonal controls of SST variability in driving intra-annual variability
 774 in gas conditions (see above, sections 3.1-3.2). The bubble terms (F_C , F_P , β) contributed
 775 relatively small errors, due to the low prevalence of elevated wind speeds (Figs. 3-4).
 776 Calculations of N_2' will, nonetheless, depend on the air-sea exchange model employed in the
 777 budget evaluations. We used the bubble-mediated model of Liang et al. (2013) because it has
 778 been validated against in-situ N_2 and noble gas measurements (here and in Emerson &
 779 Bushinsky, 2016), and was parameterized for weakly-soluble gases similar to O_2 . When possible,
 780 we recommend that future studies employ air-sea exchange parameterizations that have been
 781 validated for the region of interest.

782 An additional consideration is the influence of biological processes on $\Delta N_2/Ar$. Unlike
 783 Ar , N_2 concentrations can be altered by several bacterially-mediated processes, including surface
 784 N_2 -fixation, and subsurface or sedimentary denitrification and annamox. These processes could,
 785 in principle, impact $\Delta O_2/N_2'$ -based NCP estimates, but their influence is likely to be small under
 786 most conditions. Rates of N_2 -fixation are orders of magnitude smaller than air-sea gas fluxes
 787 over most oceanic regions, minimizing the influence of this process on $\Delta N_2/Ar$ (Figs. S7, S8). In
 788 nitrate-deplete waters of the subtropical and tropical ocean, where N_2 -fixation is most important
 789 (Deutsch et al., 2007; Gruber & Sarmiento, 1997) the upper range of N_2 -fixation rates is ~ 220
 790 $\text{mmol } N_2 \text{ m}^{-2} \text{ yr}^{-1}$ ($\sim 0.6 \text{ mmol } N_2 \text{ m}^{-2} \text{ d}^{-1}$). Elsewhere, mean estimates of N_2 -fixation in
 791 subtropical, temperate and polar waters range from about <0.01 to $0.24 \text{ mmol } N_2 \text{ m}^{-2} \text{ d}^{-1}$ (Blais et
 792 al., 2012; Sipler et al., 2017; Tang et al., 2019, 2020). Net air-sea exchange fluxes almost always
 793 exceed the maximum rate of N_2 -fixation (Fig. S8), so that any ΔN_2 anomalies produced by
 794 biological processes should be rapidly erased at wind speeds above $\sim 3 \text{ m s}^{-1}$. Neglecting the
 795 influence of other physical gas fluxes (e.g. vertical mixing), maximum rates of N_2 -fixation
 796 applied to our model will only induce a quasi-steady-state ΔN_2 anomaly larger than 0.05 % at u_{10}
 797 below 6 m s^{-1} (Fig. S8b), which only occurs consistently in a narrow latitude band near the
 798 equator. Regardless, periodic elevated sea states should rapidly erase any accumulated N_2
 799 deficits (Shigemitsu et al., 2016). Indeed, in an additional real-OSP run forced with constant
 800 global maximum N_2 -fixation rate, simulated ΔN_2 always differed from values in the base run by
 801 less than 0.05 %. We thus conclude that N_2 -fixation should not have a significant impact on the
 802 derivation of N_2' , or on $\Delta O_2/N_2'$ -based NCP estimates.

803 The influence of denitrification and annamox on surface $\Delta O_2/N_2'$ will also be small and
 804 indirect, as these processes elevate $\Delta N_2/Ar_{\text{deep}}$ (Deutsch et al., 2007; Gruber & Sarmiento, 1997;
 805 Kana et al., 1998; Tortell, 2005), but do not alter surface N_2 directly. Their contribution to
 806 potential vertical mixing of excess N_2 into the mixed layer may only be prominent in regions

807 where O₂ and nitrate depletion occurs in the upper few hundred of meters of the water column
808 (e.g. Arabian Sea, Eastern Tropical North and South Pacific, suboxic inlets and estuaries; Chang
809 et al., 2010, 2012; DeVries et al., 2012; Tortell, 2005; Wu et al., 2013) or overlying shallow
810 continental shelves where benthic and sedimentary denitrification occur (DeVries et al., 2013).
811 Taking an extreme upper limit of subsurface $\Delta N_2/Ar$ of ~ 2 -2.5 % in these regions (Chang et al.,
812 2010; 2012; Shigemitsu et al., 2016), surface $\Delta N_2/Ar$ anomalies will be less than 2.5 % (Fig. 1).
813 N₂' corrections can minimize this bias, but even without such corrections, the error associated
814 with a 2.5 % underestimation of $\Delta O_2/N_2$ may be smaller than errors associated with vertical O₂
815 mixing fluxes in continental shelf regions (see above).

816 Other processes which we have not evaluated in the present study, such as freshwater
817 input, lateral mixing and ice melt/formation can also cause divergence between ΔAr and ΔN_2
818 (e.g. Beaird et al., 2015; Crabeck et al., 2014; Eveleth et al., 2017; Hamme et al., 2019; Hamme
819 & Emerson, 2013; Loose & Jenkins, 2014; Top et al., 1988), but their contributions to surface
820 $\Delta N_2/Ar$ disequilibria, and the resulting uncertainty in $\Delta O_2/N_2$ -based NCP estimates are likely to
821 be small in most ocean regions. As our model evaluation suggests (section 3.3, above), the
822 framework we presented here captures the main drivers of inert gas and N₂ variability in oceanic
823 waters. Additional fluxes will be larger in coastal, or polar regions, but biases in NCP estimates
824 resulting from vertical O₂ fluxes or diel O₂ variability are likely to be more significant in these
825 regions (see above).

826

827 **4 Conclusions**

828 Global coverage of marine NCP estimates is constrained by the limitation of mass
829 spectrometry to obtain underway $\Delta O_2/Ar$ measurements. Recent advances in Optode and GTD
830 technology have made high-resolution $\Delta O_2/N_2$ sampling feasible, providing potential avenues to
831 expand NCP from low-cost and user-friendly instrument systems (Izett & Tortell, 2020).
832 Differences between Ar and N₂ solubility properties necessitate careful interpretation of in-situ
833 O₂/N₂ measurements in order to accurately isolate biological O₂ signatures. In the present study,
834 we used a model to evaluate the main mechanisms controlling surface water uncoupling between
835 $\Delta O_2/Ar$ and $\Delta O_2/N_2$. Critically, our model, when parameterized with relevant environmental
836 forcing and time-variable mixing terms, accurately captures the main processes driving surface
837 ocean inert gas and N₂ evolution.

838 From our numerical simulations, performed under experimental and realistic conditions,
839 we find that seasonal SST variability exerts long-term control on $\Delta O_2/Ar$ and $\Delta O_2/N_2$
840 decoupling, with transient and baseline modifications resulting from enhanced bubble fluxes
841 during periods of elevated wind-speeds, and variable vertical mixing fluxes. Due to differences
842 in the sensitivity of Ar and N₂ to SST variability and small bubble injection, nominal $\Delta N_2/Ar$
843 anomalies are generally positive over a range of conditions, so that NCP estimates derived from
844 raw $\Delta O_2/N_2$ measurements could be biased low. Fortunately, the predictability of these
845 anomalies to environmental perturbations permits corrections to ΔN_2 measurements, based on a
846 new tracer, $\Delta N_2'$, which we derived from simple MLD budget calculations performed over a
847 relevant NCP time-scale, τ_{O_2} . Applying this $\Delta N_2'$ approach using readily available reanalysis data
848 products allows us to reconcile differences between $\Delta O_2/Ar$ and $\Delta O_2/N_2$, making $\Delta O_2/N_2'$ a
849 robust NCP tracer.

850 The overall uncertainty in $\Delta O_2/N_2'$, resulting from model parameterization errors and
851 necessary simplifying assumptions, is generally smaller than other sources of uncertainty in NCP
852 calculations. Field application of the present approach will depend on the accuracy of
853 environmental data products, and assumptions about the time-variability of mixed layer
854 hydrography. Yet, even when differences between $\Delta O_2/Ar$ and $\Delta O_2/N_2'$ cannot be reduced to
855 zero, N_2' is still a valuable tracer for minimizing NCP errors based on O_2/N_2 measurements. This
856 approach is expected to be most accurate in stratified waters and during summer conditions,
857 when surface productivity is elevated, and mixing contributions to $\Delta N_2/Ar$ decoupling may be
858 neglected in N_2' calculations. In most ocean regions, N_2 -fixation, denitrification and anammox
859 will have a negligible impact on NCP estimates derived from underway $\Delta O_2/N_2'$.

860 Our work demonstrates the feasibility of deriving $\Delta O_2/N_2'$ -based NCP estimates from
861 underway O_2 and N_2 measurements and simple computations. The approach we describe here has
862 the potential to greatly expand NCP coverage from research vessels, volunteer observing
863 platforms and/or autonomous surface vehicles. This approach, combined with our upcoming field
864 validation (manuscript in preparation) constitutes a significant advance in our ability to
865 accurately quantify NCP and oceanic metabolism across a range of relevant space and time
866 spaces.

867

868 **Acknowledgments**

869 We would like to thank R. Hamme for her insightful comments on the manuscript, and for
870 sharing data used in our model simulations. S. Emerson and various groups at NOAA and DFO
871 Canada also provided data to validate the simulations. Some of the data used were collected by
872 the Canadian research icebreaker *CCGS Amundsen* and made available by the Amundsen
873 Science program, which was supported by the Canada Foundation for Innovation and Natural
874 Sciences and Engineering Research Council of Canada (NSERC). Matlab codes (including input
875 forcing data) for the model simulations and N_2' calculations presented here are provided in an
876 `O2N2_NCP_toolbox` repository at doi.org/10.5281/zenodo.4024952. These codes can be used as
877 templates for future studies, including field surveys. Codes contain scripts written by R. Izett and
878 P. Tortell, and colleagues C. Manning, D. Nicholson (github.com/dnicholson/gas_toolbox), R.
879 Hamme (web.uvic.ca/~rhamme/download.html) and others; we thank them for making their
880 contributions freely available. The output from simulations presented in this manuscript can also
881 be accessed from the same toolbox. This work was supported by NSERC through the Discovery
882 Grant and Alexander Graham Bell Canada Graduate Scholarship (CGS-D) programs, and by
883 MEOPAR and ArcticNet. We declare no conflict of interest in the production of this work.

884

885 **References**

- 886 Amundsen Science Data Collection. (2019). CTD data collected by the CCGS Amundsen in the
887 Canadian Arctic. ArcticNet Inc., Québec, Canada. Processed data. Version 1. Archived at
888 www.polardata.ca. Waterloo, Canada: Canadian Cryospheric Information Network (CCIN).
889 <https://doi.org/https://doi.org/10.5884/12713>. Accessed May 2020.
- 890 Atlas, R., Hoffman, R. N., Ardizzone, J., Leidner, S. M., Jusem, J. C., Smith, D. K., & Gombos,
891 D. (2011). A cross-calibrated, multiplatform ocean surface wind velocity product for

- 892 meteorological and oceanographic applications. *Bulletin of the American Meteorological*
893 *Society*, 92, 157–174. <https://doi.org/10.1175/2010BAMS2946.1>
- 894 Beaird, N., Straneo, F., & Jenkins, W. (2015). Spreading of Greenland meltwaters in the ocean
895 revealed by noble gases. *Geophysical Research Letters*, 42(18), 7705–7713.
896 <https://doi.org/10.1002/2015GL065003>
- 897 Bender, M. L., Kinter, S., Cassar, N., & Wanninkhof, R. (2011). Evaluating gas transfer velocity
898 parameterizations using upper ocean radon distributions. *Journal of Geophysical Research:*
899 *Oceans*, 116(2), 1–11. <https://doi.org/10.1029/2009JC005805>
- 900 Blais, M., Tremblay, J. É., Jungblut, A. D., Gagnon, J., Martin, J., Thaler, M., & Lovejoy, C.
901 (2012). Nitrogen fixation and identification of potential diazotrophs in the Canadian Arctic.
902 *Global Biogeochemical Cycles*, 26(3). <https://doi.org/10.1029/2011GB004096>
- 903 Bushinsky, S. M., & Emerson, S. (2015). Marine biological production from in situ oxygen
904 measurements on a profiling float in the subarctic Pacific Ocean. *Global Biogeochemical*
905 *Cycles*, 29, 2050–2060. <https://doi.org/10.1002/2015GB005251>
- 906 Butterworth, B. J., & Miller, S. D. (2016). Air-sea exchange of carbon dioxide in the Southern
907 Ocean and Antarctic marginal ice zone. *Geophysical Research Letters*, 43, 7223–7230.
908 <https://doi.org/10.1002/2016GL069581>
- 909 Castro de la Guardia, L., Garcia-Quintana, Y., Claret, M., Hu, X., Galbraith, E. D., & Myers, P.
910 G. (2019). Assessing the Role of High-Frequency Winds and Sea Ice Loss on Arctic
911 Phytoplankton Blooms in an Ice-Ocean-Biogeochemical Model. *Journal of Geophysical*
912 *Research: Biogeosciences*, 124(9), 2728–2750. <https://doi.org/10.1029/2018JG004869>
- 913 Chang, B. X., Devol, A. H., & Emerson, S. R. (2010). Denitrification and the nitrogen gas excess
914 in the eastern tropical South Pacific oxygen deficient zone. *Deep-Sea Research Part I:*
915 *Oceanographic Research Papers*, 57(9), 1092–1101.
916 <https://doi.org/10.1016/j.dsr.2010.05.009>
- 917 Chang, B. X., Devo, A. H., & Emerson, S. R. (2012). Fixed nitrogen loss from the eastern
918 tropical North Pacific and Arabian Sea oxygen deficient zones determined from
919 measurements of N₂:Ar. *Global Biogeochemical Cycles*, 26(3), 1–8.
920 <https://doi.org/10.1029/2011GB004207>
- 921 Chanona, M., Waterman, S., & Gratton, Y. (2018). Variability of Internal Wave-Driven Mixing
922 and Stratification in Canadian Arctic Shelf and Shelf-Slope Waters. *Journal of Geophysical*
923 *Research: Oceans*, 123(12), 9178–9195. <https://doi.org/10.1029/2018JC014342>
- 924 Crabeck, O., Delille, B., Rysgaard, S., Thomas, D. N., Geilfus, N.-X., Else, B., & Tison, J.-L.
925 (2014). First “in situ” determination of gas transport coefficients (DO₂, DAr, and DN₂)
926 from bulk gas concentration measurements (O₂, N₂, Ar) in natural sea ice. *Journal of*
927 *Geophysical Research: Oceans*, 119, 6655–6668.
928 <https://doi.org/10.1002/2014JC010105>.Received
- 929 Craig, H., & Hayward, T. (1987). Oxygen Supersaturation in the Ocean: Biological Versus
930 Physical Contributions. *Science*, 235(4785), 199–202.
931 <https://doi.org/10.1126/science.235.4785.199>
- 932 Cronin, M. F., Pellan, N. A., Emerson, S. R., & Crawford, W. R. (2015). Estimating diffusivity

- 933 from the mixed layer heat and salt balances in the North Pacific. *Journal of Geophysical*
934 *Research: Oceans*, 120, 7346–7362. <https://doi.org/10.1002/2015JC011010>
- 935 DeGrandpre, M., Evans, W., Timmermans, M., Krishfield, R., Williams, B., & Steele, M.
936 (2020). Changes in the Arctic Ocean Carbon Cycle With Diminishing Ice Cover.
937 *Geophysical Research Letters*, 47(12). <https://doi.org/10.1029/2020gl088051>
- 938 Deutsch, C., Sarmiento, J. L., Sigman, D. M., Gruber, N., & Dunne, J. P. (2007). Spatial
939 coupling of nitrogen inputs and losses in the ocean. *Nature*, 445(7124), 163–167.
940 <https://doi.org/10.1038/nature05392>
- 941 DeVries, T., Deutsch, C., Primeau, F., Chang, B., & Devol, A. (2012). Global rates of water-
942 column denitrification derived from nitrogen gas measurements. *Nature Geoscience*, 5(8),
943 547–550. <https://doi.org/10.1038/ngeo1515>
- 944 DeVries, T., Deutsch, C., Rafter, P. A., & Primeau, F. (2013). Marine denitrification rates
945 determined from a global 3-D inverse model. *Biogeosciences*, 10(4), 2481–2496.
946 <https://doi.org/10.5194/bg-10-2481-2013>
- 947 Emerson, S., & Bushinsky, S. (2016). The role of bubbles during air-sea gas exchange. *Journal*
948 *of Geophysical Research: Oceans*, 121(6), 4360–4376.
949 <https://doi.org/10.1002/2016JC011744>
- 950 Emerson, S., & Stump, C. (2010). Net biological oxygen production in the ocean-II: Remote in
951 situ measurements of O₂ and N₂ in subarctic pacific surface waters. *Deep-Sea Research*
952 *Part I: Oceanographic Research Papers*, 57, 1255–1265.
953 <https://doi.org/10.1016/j.dsr.2010.06.001>
- 954 Emerson, S., White, M. R. T., Stump, C., & Bushinsky, S. M. (2017). Salinity and other
955 variables collected from time series observations using Bubble type equilibrator for
956 autonomous carbon dioxide (CO₂) measurement, Carbon dioxide (CO₂) gas analyzer and
957 other instruments from MOORINGS_PAPA_145W_50N. NOAA National Centers for
958 Environmental Information. Dataset.
959 https://doi.org/https://doi.org/10.3334/cdiac/otg.tsm.papa_145w_50n_o2_n2.
- 960 Emerson, S., Yang, B., White, M., & Cronin, M. (2019). Air-Sea Gas Transfer: Determining
961 Bubble Fluxes With In Situ N₂ Observations. *Journal of Geophysical Research: Oceans*,
962 124(4), 2716–2727. <https://doi.org/10.1029/2018JC014786>
- 963 Eveleth, R., Timmermans, M.-L., & Cassar, N. (2014). Physical and biological controls on
964 oxygen saturation variability in the upper Arctic Ocean. *Journal of Geophysical Research:*
965 *Oceans*, 119(11), 7420–7432. <https://doi.org/https://doi.org/10.1002/2014JC009816>
- 966 Eveleth, R., Cassar, N., Doney, S. C., Munro, D. R., & Sweeney, C. (2017). Biological and
967 physical controls on O₂/Ar, Ar and pCO₂ variability at the Western Antarctic Peninsula and
968 in the Drake Passage. *Deep-Sea Research Part II*, 139, 77–88.
969 <https://doi.org/10.1016/j.dsr2.2016.05.002>
- 970 Fassbender, A. J., Sabine, C. L., & Cronin, M. F. (2016). Net community production and
971 calcification from 7 years of NOAA Station Papa Moring measurements. *Global*
972 *Biogeochemical Cycles*, 30, 250–267. <https://doi.org/10.1002/2015GB005205>
- 973 Garcia, H. E., & Gordon, L. I. (1993). Erratum: Oxygen solubility in seawater: better fitting

- 974 equations. *Limnology and Oceanography*, 38, 656.
- 975 Giesbrecht, K. E., Hamme, R. C., & Emerson, S. R. (2012). Biological productivity along Line P
976 in the subarctic northeast Pacific: In situ versus incubation-based methods. *Global*
977 *Biogeochemical Cycles*, 26(GB3028). <https://doi.org/10.1029/2012GB004349>
- 978 Gordon, C., Fennel, K., Richards, C., Shay, L. K., & Brewster, J. K. (2020). Can ocean
979 community production and respiration be determined by measuring high-frequency oxygen
980 profiles from autonomous floats? *Biogeosciences Discuss*, (Preprint).
981 <https://doi.org/10.5194/bg-2020-119>
- 982 Gruber, N., & Sarmiento, J. L. (1997). Global patterns of marine nitrogen fixation and
983 denitrification. *Global Biogeochemical Cycles*, 11(2), 235–266.
- 984 Hamme, R. C., & Emerson, S. R. (2002). Mechanisms controlling the global oceanic distribution
985 of the inert gases argon, nitrogen and neon. *Geophysical Research Letters*, 29(23), 1–4.
986 <https://doi.org/10.1029/2002GL015273>
- 987 Hamme, R. C., & Emerson, S. R. (2004). The solubility of neon, nitrogen and argon in distilled
988 water and seawater. *Deep-Sea Research Part I*, 51, 1517–1528.
989 <https://doi.org/10.1016/j.dsr.2004.06.009>
- 990 Hamme, R. C., & Emerson, S. R. (2006). Constraining bubble dynamics and mixing with
991 dissolved gases: Implications for productivity measurements by oxygen mass balance.
992 *Journal of Marine Research*, 64, 73–95. <https://doi.org/10.1357/002224006776412322>
- 993 Hamme, R. C., & Emerson, S. R. (2013). Deep-sea nutrient loss inferred from the marine
994 dissolved N₂/Ar ratio. *Geophysical Research Letters*, 40(6), 1149–1153.
995 <https://doi.org/10.1002/grl.50275>
- 996 Hamme, R. C., & Severinghaus, J. P. (2007). Trace gas disequilibria during deep-water
997 formation. *Deep-Sea Research Part I: Oceanographic Research Papers*, 54(6), 939–950.
998 <https://doi.org/10.1016/j.dsr.2007.03.008>
- 999 Hamme, R. C., Cassar, N., Lance, V. P., Vaillancourt, R. D., Bender, M. L., Strutton, P. G., et al.
1000 (2012). Dissolved O₂/Ar and other methods reveal rapid changes in productivity during a
1001 Lagrangian experiment in the Southern Ocean. *Journal of Geophysical Research*,
1002 117(C00F12). <https://doi.org/10.1029/2011JC007046>
- 1003 Hamme, R. C., Emerson, S. R., Severinghaus, J. P., Long, M. C., & Yashayaev, I. (2017). Using
1004 Noble Gas Measurements to Derive Air-Sea Process Information and Predict Physical Gas
1005 Saturations. *Geophysical Research Letters*, 44(19), 9901–9909.
1006 <https://doi.org/10.1002/2017GL075123>
- 1007 Hamme, R. C., Nicholson, D. P., Jenkins, W. J., & Emerson, S. R. (2019). Using Noble Gases to
1008 Assess the Ocean's Carbon Pumps. *Annual Review of Marine Science*, 11(18), 1–29.
1009 <https://doi.org/10.1146/annurev-marine-121916-063604>
- 1010 Hartmann, D. L. (1994). The ocean general circulation and climate. In *Global Physical*
1011 *Climatology* (pp. 171–203). San Diego, CA: Academic Press.
- 1012 Howard, E., Emerson, S., Bushinsky, S., & Stump, C. (2010). The role of net community
1013 production in air-sea carbon fluxes at the North Pacific subarctic-subtropical boundary
1014 region. *Limnology and Oceanography*, 55(6), 2585–2596.

- 1015 <https://doi.org/10.4319/lo.2010.55.6.2585>
- 1016 Islam, F., DeGrandpre, M., Beatty, C., Krishfield, R., & Toole, J. (2016). Gas exchange of CO₂
1017 and O₂ in partially ice-covered regions of the Arctic Ocean investigated using in situ
1018 sensors. *IOP Conference Series: Earth and Environmental Science*, 35(012018).
1019 <https://doi.org/10.1088/1755-1315/35/1/012018>
- 1020 Ito, T., & Deutsch, C. (2006). Understanding the saturation state of argon in the thermocline: The
1021 role of air-sea gas exchange and diapycnal mixing. *Global Biogeochemical Cycles*, 20(3),
1022 1–15. <https://doi.org/10.1029/2005GB002655>
- 1023 Izett, R., & Tortell, P. (2020). The Pressure of In Situ Gases Instrument (PIGI) for Autonomous
1024 Shipboard Measurement of Dissolved O₂ and N₂ in Surface Ocean Waters. *Oceanography*,
1025 33(2). <https://doi.org/10.5670/oceanog.2020.214>
- 1026 Izett, R., Manning, C. C., Hamme, R. C., & Tortell, P. D. (2018). Refined estimates of net
1027 community production in the Subarctic Northeast Pacific derived from ΔO₂/Ar
1028 measurements with N₂O-based corrections for vertical mixing. *Global Biogeochemical*
1029 *Cycles*, 32, 326–350. <https://doi.org/https://doi.org/10.1002/2017GB005792>
- 1030 Johnson, K. S., Plant, J. N., Dunne, J. P., Talley, L. D., & Sarmiento, J. L. (2017). Annual nitrate
1031 drawdown observed by SOCCOM profiling floats and the relationship to annual net
1032 community production. *Journal of Geophysical Research: Oceans*, 122(8), 6668–6683.
1033 <https://doi.org/10.1002/2017JC012839>
- 1034 Jonsson, B. F., Doney, S. C., Dunne, J., & Bender, M. (2013). Evaluation of the Southern Ocean
1035 O₂/Ar-based NCP estimates in a model framework. *Journal of Geophysical Research:*
1036 *Biogeosciences*, 118, 385–399. <https://doi.org/10.1002/jgrg.20032>
- 1037 Juranek, L., Takahashi, T., Mathis, J., & Pickart, R. (2019). Significant Biologically Mediated
1038 CO₂ Uptake in the Pacific Arctic During the Late Open Water Season. *Journal of*
1039 *Geophysical Research: Oceans*, 124(2), 1–23. <https://doi.org/10.1029/2018JC014568>
- 1040 Kaiser, J., Reuer, M. K., Barnett, B., & Bender, M. L. (2005). Marine productivity estimates
1041 from continuous O₂/Ar ratio measurements by membrane inlet mass spectrometry.
1042 *Geophysical Research Letters*, 32(L19605). <https://doi.org/10.1029/2005GL023459>
- 1043 Kalnay, E., Kanamitsu, M., Kistler, R., Collins, W., Deaven, D., Gandin, L., et al. (1996). The
1044 NCEP/NCAR 40-year reanalysis project. *Bulletin of the American Meteorological Society*,
1045 77, 437–471. [https://doi.org/10.1175/1520-0477\(1996\)077<0437:TNYRP>2.0.CO;2](https://doi.org/10.1175/1520-0477(1996)077<0437:TNYRP>2.0.CO;2)
- 1046 Kana, T. M., Sullivan, M. B., Cornwell, J. C., & Groszkowski, K. M. (1998). Denitrification in
1047 estuarine sediments determined by membrane inlet mass spectrometry. *Limnology and*
1048 *Oceanography*, 43(2), 334–339. <https://doi.org/10.4319/lo.1998.43.2.0334>
- 1049 Liang, J.-H. H., Deutsch, C., McWilliams, J. C., Baschek, B., Sullivan, P. P., & Chiba, D.
1050 (2013). Parameterizing bubble-mediated air-sea gas exchange and its effect on ocean
1051 ventilation. *Global Biogeochemical Cycles*, 27(3), 894–905.
1052 <https://doi.org/10.1002/gbc.20080>
- 1053 Liang, J. H., Emerson, S. R., D’Asaro, E. A., McNeil, C. L., Harcourt, R. R., Sullivan, P. P., et
1054 al. (2017). On the role of sea-state in bubble-mediated air-sea gas flux during a winter
1055 storm. *Journal of Geophysical Research: Oceans*, 122(4), 2671–2685.

- 1056 <https://doi.org/10.1002/2016JC012408>
- 1057 Lockwood, D., Quay, P. D., Kavanaugh, M. T., Juranek, L. W., & Feely, R. A. (2012). High-
1058 resolution estimates of net community production and air-sea CO₂ flux in the northeast
1059 Pacific. *Global Biogeochemical Cycles*, 26(GB4010).
1060 <https://doi.org/10.1029/2012GB004380>
- 1061 Loose, B., & Jenkins, W. J. (2014). The five stable noble gases are sensitive unambiguous tracers
1062 of glacial meltwater. *Geophysical Research Letters*, 41, 2835–2841.
1063 <https://doi.org/doi:10.1002/2013GL058804>
- 1064 Loose, B., McGillis, W. R., Perovich, D., Zappa, C. J., & Schlosser, P. (2014). A parameter
1065 model of gas exchange for the seasonal sea ice zone. *Ocean Science*, 10(1), 17–28.
1066 <https://doi.org/10.5194/os-10-17-2014>
- 1067 Manning, C. C., Stanley, R. H. R., Nicholson, D. P., Loose, B., Lovely, A., Schlosser, P., &
1068 Hatcher, B. G. (2017). Changes in gross oxygen production, net oxygen production, and air-
1069 water gas exchange during seasonal ice melt in the Bras d’Or Lake, a Canadian estuary.
1070 *Biogeosciences Discussions*. <https://doi.org/10.5194/bg-2017-428>
- 1071 McNeil, C., D’Asaro, E., Johnson, B., & Horn, M. (2006a). A gas tension device with response
1072 times of minutes. *Journal of Atmospheric and Oceanic Technology*, 23(11), 1539–1558.
1073 <https://doi.org/10.1175/JTECH1974.1>
- 1074 McNeil, C., Katz, D. R., Ward, B., McGillis, W. R., & Johnson, B. D. (2006b). A method to
1075 estimate net community metabolism from profiles of dissolved O₂ and N₂. *Hydrobiologia*,
1076 571(1), 181–190. <https://doi.org/10.1007/s10750-006-0236-7>
- 1077 McNeil, C. L., Johnson, B. D., & Farmer, D. M. (1995). In situ measurement of dissolved
1078 nitrogen and oxygen in the ocean. *Deep-Sea Research Part I*, 42(5), 819–826.
1079 [https://doi.org/10.1016/0967-0637\(95\)97829-W](https://doi.org/10.1016/0967-0637(95)97829-W)
- 1080 Mordy, C. W., Cokelet, E. D., Robertis, A. De, Jenkins, R., Kuhn, C. E., Lawrence-Salvas, N., et
1081 al. (2017). Advances in Ecosystem Research: Saildrone Surveys of Oceanography, Fish,
1082 and Marine Mammals in the Bering Sea. *Oceanography*, 30(2), 113–115.
- 1083 Munro, D. R., Quay, P. D., Juranek, L. W., & Goericke, R. (2013). Biological production rates
1084 off the Southern California coast estimated from triple O₂ isotopes and O₂ : Ar gas ratios.
1085 *Limnology and Oceanography*, 58(4), 1312–1328.
1086 <https://doi.org/10.4319/lo.2013.58.4.1312>
- 1087 Nicholson, D., Emerson, S., Caillon, N., Jouzel, J., & Hamme, R. C. (2010). Constraining
1088 ventilation during deepwater formation using deep ocean measurements of the dissolved gas
1089 ratios 40 Ar/ 36 Ar, N₂ /Ar, and Kr/Ar. *Journal of Geophysical Research*, 115(C11015), 1–
1090 15. <https://doi.org/10.1029/2010jc006152>
- 1091 Nilsson, E. D., Rannik, Ü., Swietlicki, E., Leck, C., Aalto, P. P., Zhou, J., & Norman, M. (2001).
1092 Turbulent aerosol fluxes over the Arctic Ocean 2. Wind-driven sources from the sea.
1093 *Journal of Geophysical Research*, 106(D23), 32139–32154.
- 1094 Palevsky, H. I., Quay, P. D., Lockwood, D. E., & Nicholson, D. P. (2016). The annual cycle of
1095 gross primary production, net community production, and export efficiency across the
1096 North Pacific Ocean. *Global Biogeochemical Cycles*, 30(2), 361–380.

- 1097 <https://doi.org/10.1002/2015GB005318>
- 1098 Pelland, N. A., Eriksen, C. C., Emerson, S. R., & Cronin, M. F. (2018). Seaglider surveys at
1099 Ocean Station Papa: Oxygen kinematics and upper-ocean metabolism. *Journal of*
1100 *Geophysical Research: Oceans*, 1–20. <https://doi.org/10.1029/2018JC014091>
- 1101 Plant, J. N., Johnson, K. S., Sakamoto, C. M., Jannasch, H. W., Coletti, L. J., Riser, S. C., &
1102 Swift, D. D. (2016). Net community production at Ocean Station Papa observed with nitrate
1103 and oxygen sensors on profiling floats. *Global Biogeochemical Cycles*, 30, 859–879.
1104 <https://doi.org/10.1002/2015GB005349>.Received
- 1105 Reed, A., McNeil, C., D’Asaro, E., Altabet, M., Bourbonnais, A., & Johnson, B. (2018). A gas
1106 tension device for the mesopelagic zone. *Deep-Sea Research Part I*, 139(2018), 68–78.
1107 <https://doi.org/10.1016/j.dsr.2018.07.007>
- 1108 Reynolds, R. W., Smith, T. M., Liu, C., Chelton, D. B., Casey, K. S., & Schlax, M. G. (2007).
1109 Daily High-Resolution-Blended Analyses for Sea Surface Temperature. *Journal of Climate*,
1110 20, 5473–5496.
- 1111 Rosengard, S. Z., Izett, R. W., Burt, W. J., Schuback, N., & Tortell, P. D. (2020). Decoupling of
1112 O₂ / Ar and particulate organic carbon dynamics in nearshore surface ocean waters.
1113 *Biogeosciences*, 17, 3277–3298. Retrieved from <https://doi.org/10.5194/bg-17-3277-2020>
- 1114 Scheifele, B., Waterman, S., Merckelbach, L., & Carpenter, J. R. (2018). Measuring the
1115 Dissipation Rate of Turbulent Kinetic Energy in Strongly Stratified, Low-Energy
1116 Environments: A Case Study From the Arctic Ocean. *Journal of Geophysical Research:*
1117 *Oceans*, 123, 5459–5480. <https://doi.org/10.1029/2017JC013731>
- 1118 Schmidtko, S., Johnson, G. C., & Lyman, J. M. (2013). MIMOC: A global monthly isopycnal
1119 upper-ocean climatology with mixed layers. *Journal of Geophysical Research: Oceans*,
1120 118, 1658–1672.
- 1121 Shigemitsu, M., Gruber, N., Oka, A., & Yamanaka, Y. (2016). Potential use of the N₂/Ar ratio as
1122 a constraint on the oceanic fixed nitrogen loss. *Global Biogeochemical Cycles*, 30, 576–594.
1123 <https://doi.org/10.1111/1462-2920.13280>
- 1124 Sipler, R. E., Gong, D., Baer, S. E., Sanderson, M. P., Roberts, Q. N., Mulholland, M. R., &
1125 Bronk, D. A. (2017). Preliminary estimates of the contribution of Arctic nitrogen fixation to
1126 the global nitrogen budget. *Limnology and Oceanography Letters*, 2(5), 159–166.
1127 <https://doi.org/10.1002/lol2.10046>
- 1128 Steiner, N., Vagle, S., Denman, K. L., & McNeil, C. (2007). Oxygen and nitrogen cycling in the
1129 northeast Pacific - Simulations and observations at Station Papa in 2003/2004. *Journal of*
1130 *Marine Research*, 65(3), 441–469. <https://doi.org/10.1357/002224007781567658>
- 1131 Tang, W., Wang, S., Fonseca-Batista, D., Dehairs, F., Gifford, S., Gonzalez, A. G., et al. (2019).
1132 Revisiting the distribution of oceanic N₂ fixation and estimating diazotrophic contribution
1133 to marine production. *Nature Communications*, 10(1), 1–10.
1134 <https://doi.org/10.1038/s41467-019-08640-0>
- 1135 Tang, W., Cerdán-García, E., Berthelot, H., Polyviou, D., Wang, S., Baylay, A., et al. (2020).
1136 New insights into the distributions of nitrogen fixation and diazotrophs revealed by high-
1137 resolution sensing and sampling methods. *ISME Journal*. <https://doi.org/10.1038/s41396->

- 1138 020-0703-6
- 1139 Teeter, L., Hamme, R. C., Ianson, D., & Bianucci, L. (2018). Accurate Estimation of Net
1140 Community Production From O₂/Ar Measurements. *Global Biogeochemical Cycles*, 1–19.
1141 <https://doi.org/10.1029/2017GB005874>
- 1142 Tengberg, A., Hovdenes, J., Andersson, H. J., Brocandel, O., Diaz, R., Hebert, D., et al. (2006).
1143 Evaluation of a lifetime-based optode to measure oxygen in aquatic systems. *Limnology and*
1144 *Oceanography: Methods*, 4(2), 7–17. <https://doi.org/10.4319/lom.2006.4.7>
- 1145 Top, Z., Martin, S., & Becker, P. (1988). A laboratory study of dissolved noble gas anomaly due
1146 to ice formation. *Geophysical Research Letters*, 15(8), 796–799.
- 1147 Tortell, P. D. (2005). Dissolved gas measurements in oceanic waters made by membrane inlet
1148 mass spectrometry. *Limnology and Oceanography: Methods*, 3, 24–37.
1149 <https://doi.org/10.4319/lom.2005.3.24>
- 1150 Tortell, P. D., Bittig, H. C., Körtzinger, A., Jones, E. M., & Hoppema, M. (2015). Biological and
1151 physical controls on N₂, O₂, and CO₂ distributions in contrasting Southern Ocean surface
1152 waters. *Global Biogeochemical Cycles*, 29, 994–1013.
1153 <https://doi.org/10.1002/2014GB004975>
- 1154 Ulfsbo, A., Cassar, N., Korhonen, M., van Heuven, S., Hoppema, M., Kattner, G., & Anderson,
1155 L. G. (2014). Late summer net community production in the central Arctic Ocean using
1156 multiple approaches. *Global Biogeochemical Cycles*, 28, 1129–1148.
1157 <https://doi.org/10.1002/2014GB004833>
- 1158 Voermans, J. J., Babanin, A. V., Thomson, J., Smith, M. M., & Shen, H. H. (2019). Wave
1159 Attenuation by Sea Ice Turbulence. *Geophysical Research Letters*, 46(12), 6796–6803.
1160 <https://doi.org/10.1029/2019GL082945>
- 1161 Wang, S., Kranz, S. A., Kelly, T. B., Song, H., Stukel, M. R., & Cassar, N. (2020). Lagrangian
1162 Studies of Net Community Production: The Effect of Diel and Multiday Nonsteady State
1163 Factors and Vertical Fluxes on O₂/Ar in a Dynamic Upwelling Region. *Journal of*
1164 *Geophysical Research: Biogeosciences*, 125(6), 1–19.
1165 <https://doi.org/10.1029/2019jg005569>
- 1166 Wanninkhof, R. (2014). Relationship between wind speed and gas exchange over the ocean
1167 revisited. *Limnology and Oceanography: Methods*, 12(6), 351–362.
1168 <https://doi.org/10.1029/92JC00188>
- 1169 Weeding, B., & Trull, T. W. (2014). Hourly oxygen and total gas tension measurements at the
1170 Southern Ocean Time Series site reveal winter ventilation and spring net community
1171 production. *Journal of Geophysical Research: Oceans*, 119, 348–358.
1172 <https://doi.org/10.1002/2013JC009302>
- 1173 Weiss, R. F. (1970). The solubility of nitrogen, oxygen and argon in water and seawater. *Deep Sea*
1174 *Research*, 17(4), 721–735.
- 1175 Whalen, C. B., Talley, L. D., & MacKinnon, J. A. (2012). Spatial and temporal variability of
1176 global ocean mixing inferred from Argo profiles. *Geophysical Research Letters*, 39(17).
1177 <https://doi.org/10.1029/2012GL053196>
- 1178 Wise, D. L., & Houghton, G. (1966). The diffusion coefficients of ten slightly soluble gases in

- 1179 water at 10–60°C. *Chemical Engineering Science*, 21(11), 999–1010.
 1180 [https://doi.org/10.1016/0009-2509\(66\)85096-0](https://doi.org/10.1016/0009-2509(66)85096-0)
- 1181 Woolf, D. K., & Thorpe, S. A. (1991). Bubbles and the air-sea exchange of gases in near-
 1182 saturation conditions. *Journal of Marine Research*, 49, 435–466.
 1183 <https://doi.org/10.1357/002224091784995765>
- 1184 Wu, J., Chen, N., Hong, H., Lu, T., Wang, L., & Chen, Z. (2013). Direct measurement of
 1185 dissolved N₂ and denitrification along a subtropical river-estuary gradient, China. *Marine*
 1186 *Pollution Bulletin*, 66(2013), 125–134. <https://doi.org/10.1016/j.marpolbul.2012.10.020>
- 1187 Yang, B., Emerson, S. R., & Bushinsky, S. M. (2017). Annual net community production in the
 1188 subtropical Pacific Ocean from in-situ oxygen measurements on profiling floats. *Global*
 1189 *Biogeochemical Cycles*, 31, 728–744. <https://doi.org/10.1002/2016GB005545>
- 1190 Zhou, J., Delille, B., Brabant, F., & Tison, J. L. (2014). Insights into oxygen transport and net
 1191 community production in sea ice from oxygen, nitrogen and argon concentrations.
 1192 *Biogeosciences*, 11, 5007–5020. <https://doi.org/10.5194/bg-11-5007-2014>
- 1193
 1194
- 1195 **Supporting Information References**
- 1196 Amundsen Science Data Collection. (2019). CTD data collected by the CCGS Amundsen in the
 1197 Canadian Arctic. ArcticNet Inc., Québec, Canada. Processed data. Version 1. Archived at
 1198 www.polardata.ca. Waterloo, Canada: Canadian Cryospheric Information Network (CCIN).
 1199 <https://doi.org/https://doi.org/10.5884/12713>. Accessed May 2020.
- 1200 Atlas, R., Hoffman, R. N., Ardizzone, J., Leidner, S. M., Jusem, J. C., Smith, D. K., & Gombos,
 1201 D. (2011). A cross-calibrated, multiplatform ocean surface wind velocity product for
 1202 meteorological and oceanographic applications. *Bulletin of the American Meteorological*
 1203 *Society*, 92, 157–174. <https://doi.org/10.1175/2010BAMS2946.1>
- 1204 Beaird, N., Straneo, F., & Jenkins, W. (2015). Spreading of Greenland meltwaters in the ocean
 1205 revealed by noble gases. *Geophysical Research Letters*, 42(18), 7705–7713.
 1206 <https://doi.org/10.1002/2015GL065003>
- 1207 Bender, M. L., Kinter, S., Cassar, N., & Wanninkhof, R. (2011). Evaluating gas transfer velocity
 1208 parameterizations using upper ocean radon distributions. *Journal of Geophysical Research:*
 1209 *Oceans*, 116(2), 1–11. <https://doi.org/10.1029/2009JC005805>
- 1210 Blais, M., Tremblay, J. É., Jungblut, A. D., Gagnon, J., Martin, J., Thaler, M., & Lovejoy, C.
 1211 (2012). Nitrogen fixation and identification of potential diazotrophs in the Canadian Arctic.
 1212 *Global Biogeochemical Cycles*, 26(3). <https://doi.org/10.1029/2011GB004096>
- 1213 Bushinsky, S. M., & Emerson, S. (2015). Marine biological production from in situ oxygen
 1214 measurements on a profiling float in the subarctic Pacific Ocean. *Global Biogeochemical*
 1215 *Cycles*, 29, 2050–2060. <https://doi.org/10.1002/2015GB005251>
- 1216 Butterworth, B. J., & Miller, S. D. (2016). Air-sea exchange of carbon dioxide in the Southern
 1217 Ocean and Antarctic marginal ice zone. *Geophysical Research Letters*, 43, 7223–7230.
 1218 <https://doi.org/10.1002/2016GL069581>

- 1219 Castro de la Guardia, L., Garcia-Quintana, Y., Claret, M., Hu, X., Galbraith, E. D., & Myers, P.
1220 G. (2019). Assessing the Role of High-Frequency Winds and Sea Ice Loss on Arctic
1221 Phytoplankton Blooms in an Ice-Ocean-Biogeochemical Model. *Journal of Geophysical*
1222 *Research: Biogeosciences*, 124(9), 2728–2750. <https://doi.org/10.1029/2018JG004869>
- 1223 Chang, B. X., Devol, A. H., & Emerson, S. R. (2010). Denitrification and the nitrogen gas excess
1224 in the eastern tropical South Pacific oxygen deficient zone. *Deep-Sea Research Part I:*
1225 *Oceanographic Research Papers*, 57(9), 1092–1101.
1226 <https://doi.org/10.1016/j.dsr.2010.05.009>
- 1227 Chang, B. X., Devo, A. H., & Emerson, S. R. (2012). Fixed nitrogen loss from the eastern
1228 tropical North Pacific and Arabian Sea oxygen deficient zones determined from
1229 measurements of N₂:Ar. *Global Biogeochemical Cycles*, 26(3), 1–8.
1230 <https://doi.org/10.1029/2011GB004207>
- 1231 Chanona, M., Waterman, S., & Gratton, Y. (2018). Variability of Internal Wave-Driven Mixing
1232 and Stratification in Canadian Arctic Shelf and Shelf-Slope Waters. *Journal of Geophysical*
1233 *Research: Oceans*, 123(12), 9178–9195. <https://doi.org/10.1029/2018JC014342>
- 1234 Crabeck, O., Delille, B., Rysgaard, S., Thomas, D. N., Geilfus, N.-X., Else, B., & Tison, J.-L.
1235 (2014). First “in situ” determination of gas transport coefficients (DO₂, DAr, and DN₂)
1236 from bulk gas concentration measurements (O₂, N₂, Ar) in natural sea ice. *Journal of*
1237 *Geophysical Research: Oceans*, 119, 6655–6668.
1238 <https://doi.org/10.1002/2014JC010105>.Received
- 1239 Craig, H., & Hayward, T. (1987). Oxygen Supersaturation in the Ocean: Biological Versus
1240 Physical Contributions. *Science*, 235(4785), 199–202.
1241 <https://doi.org/10.1126/science.235.4785.199>
- 1242 Cronin, M. F., Pellan, N. A., Emerson, S. R., & Crawford, W. R. (2015). Estimating diffusivity
1243 from the mixed layer heat and salt balances in the North Pacific. *Journal of Geophysical*
1244 *Research: Oceans*, 120, 7346–7362. <https://doi.org/10.1002/2015JC011010>
- 1245 DeGrandpre, M., Evans, W., Timmermans, M., Krishfield, R., Williams, B., & Steele, M.
1246 (2020). Changes in the Arctic Ocean Carbon Cycle With Diminishing Ice Cover.
1247 *Geophysical Research Letters*, 47(12). <https://doi.org/10.1029/2020gl088051>
- 1248 Deutsch, C., Sarmiento, J. L., Sigman, D. M., Gruber, N., & Dunne, J. P. (2007). Spatial
1249 coupling of nitrogen inputs and losses in the ocean. *Nature*, 445(7124), 163–167.
1250 <https://doi.org/10.1038/nature05392>
- 1251 DeVries, T., Deutsch, C., Primeau, F., Chang, B., & Devol, A. (2012). Global rates of water-
1252 column denitrification derived from nitrogen gas measurements. *Nature Geoscience*, 5(8),
1253 547–550. <https://doi.org/10.1038/ngeo1515>
- 1254 DeVries, T., Deutsch, C., Rafter, P. A., & Primeau, F. (2013). Marine denitrification rates
1255 determined from a global 3-D inverse model. *Biogeosciences*, 10(4), 2481–2496.
1256 <https://doi.org/10.5194/bg-10-2481-2013>
- 1257 Emerson, S., & Bushinsky, S. (2016). The role of bubbles during air-sea gas exchange. *Journal*
1258 *of Geophysical Research: Oceans*, 121(6), 4360–4376.
1259 <https://doi.org/10.1002/2016JC011744>

- 1260 Emerson, S., & Stump, C. (2010). Net biological oxygen production in the ocean-II: Remote in
1261 situ measurements of O₂ and N₂ in subarctic pacific surface waters. *Deep-Sea Research*
1262 *Part I: Oceanographic Research Papers*, 57, 1255–1265.
1263 <https://doi.org/10.1016/j.dsr.2010.06.001>
- 1264 Emerson, S., White, M. R. T., Stump, C., & Bushinsky, S. M. (2017). Salinity and other
1265 variables collected from time series observations using Bubble type equilibrator for
1266 autonomous carbon dioxide (CO₂) measurement, Carbon dioxide (CO₂) gas analyzer and
1267 other instruments from MOORINGS_PAPA_145W_50N. NOAA National Centers for
1268 Environmental Information. Dataset.
1269 https://doi.org/https://doi.org/10.3334/cdiac/otg.tsm.papa_145w_50n_o2_n2.
- 1270 Emerson, S., Yang, B., White, M., & Cronin, M. (2019). Air-Sea Gas Transfer: Determining
1271 Bubble Fluxes With In Situ N₂ Observations. *Journal of Geophysical Research: Oceans*,
1272 124(4), 2716–2727. <https://doi.org/10.1029/2018JC014786>
- 1273 Eveleth, R., Timmermans, M.-L., & Cassar, N. (2014). Physical and biological controls on
1274 oxygen saturation variability in the upper Arctic Ocean. *Journal of Geophysical Research:*
1275 *Oceans*, 119(11), 7420–7432. <https://doi.org/https://doi.org/10.1002/2014JC009816>
- 1276 Eveleth, R., Cassar, N., Doney, S. C., Munro, D. R., & Sweeney, C. (2017). Biological and
1277 physical controls on O₂/Ar, Ar and pCO₂ variability at the Western Antarctic Peninsula and
1278 in the Drake Passage. *Deep-Sea Research Part II*, 139, 77–88.
1279 <https://doi.org/10.1016/j.dsr2.2016.05.002>
- 1280 Fassbender, A. J., Sabine, C. L., & Cronin, M. F. (2016). Net community production and
1281 calcification from 7 years of NOAA Station Papa Moring measurements. *Global*
1282 *Biogeochemical Cycles*, 30, 250–267. <https://doi.org/10.1002/2015GB005205>
- 1283 Garcia, H. E., & Gordon, L. I. (1993). Erratum: Oxygen solubility in seawater: better fitting
1284 equations. *Limnology and Oceanography*, 38, 656.
- 1285 Giesbrecht, K. E., Hamme, R. C., & Emerson, S. R. (2012). Biological productivity along Line P
1286 in the subarctic northeast Pacific: In situ versus incubation-based methods. *Global*
1287 *Biogeochemical Cycles*, 26(GB3028). <https://doi.org/10.1029/2012GB004349>
- 1288 Gordon, C., Fennel, K., Richards, C., Shay, L. K., & Brewster, J. K. (2020). Can ocean
1289 community production and respiration be determined by measuring high-frequency oxygen
1290 profiles from autonomous floats? *Biogeosciences Discuss*, (Preprint).
1291 <https://doi.org/10.5194/bg-2020-119>
- 1292 Gruber, N., & Sarmiento, J. L. (1997). Global patterns of marine nitrogen fixation and
1293 denitrification. *Global Biogeochemical Cycles*, 11(2), 235–266.
- 1294 Hamme, R. C., & Emerson, S. R. (2002). Mechanisms controlling the global oceanic distribution
1295 of the inert gases argon, nitrogen and neon. *Geophysical Research Letters*, 29(23), 1–4.
1296 <https://doi.org/10.1029/2002GL015273>
- 1297 Hamme, R. C., & Emerson, S. R. (2004). The solubility of neon, nitrogen and argon in distilled
1298 water and seawater. *Deep-Sea Research Part I*, 51, 1517–1528.
1299 <https://doi.org/10.1016/j.dsr.2004.06.009>
- 1300 Hamme, R. C., & Emerson, S. R. (2006). Constraining bubble dynamics and mixing with

- 1301 dissolved gases: Implications for productivity measurements by oxygen mass balance.
1302 *Journal of Marine Research*, 64, 73–95. <https://doi.org/10.1357/002224006776412322>
- 1303 Hamme, R. C., & Emerson, S. R. (2013). Deep-sea nutrient loss inferred from the marine
1304 dissolved N₂/Ar ratio. *Geophysical Research Letters*, 40(6), 1149–1153.
1305 <https://doi.org/10.1002/grl.50275>
- 1306 Hamme, R. C., & Severinghaus, J. P. (2007). Trace gas disequilibria during deep-water
1307 formation. *Deep-Sea Research Part I: Oceanographic Research Papers*, 54(6), 939–950.
1308 <https://doi.org/10.1016/j.dsr.2007.03.008>
- 1309 Hamme, R. C., Cassar, N., Lance, V. P., Vaillancourt, R. D., Bender, M. L., Strutton, P. G., et al.
1310 (2012). Dissolved O₂/Ar and other methods reveal rapid changes in productivity during a
1311 Lagrangian experiment in the Southern Ocean. *Journal of Geophysical Research*,
1312 117(C00F12). <https://doi.org/10.1029/2011JC007046>
- 1313 Hamme, R. C., Emerson, S. R., Severinghaus, J. P., Long, M. C., & Yashayaev, I. (2017). Using
1314 Noble Gas Measurements to Derive Air-Sea Process Information and Predict Physical Gas
1315 Saturations. *Geophysical Research Letters*, 44(19), 9901–9909.
1316 <https://doi.org/10.1002/2017GL075123>
- 1317 Hamme, R. C., Nicholson, D. P., Jenkins, W. J., & Emerson, S. R. (2019). Using Noble Gases to
1318 Assess the Ocean’s Carbon Pumps. *Annual Review of Marine Science*, 11(18), 1–29.
1319 <https://doi.org/10.1146/annurev-marine-121916-063604>
- 1320 Hartmann, D. L. (1994). The ocean general circulation and climate. In *Global Physical*
1321 *Climatology* (pp. 171–203). San Diego, CA: Academic Press.
- 1322 Howard, E., Emerson, S., Bushinsky, S., & Stump, C. (2010). The role of net community
1323 production in air-sea carbon fluxes at the North Pacific subarctic-subtropical boundary
1324 region. *Limnology and Oceanography*, 55(6), 2585–2596.
1325 <https://doi.org/10.4319/lo.2010.55.6.2585>
- 1326 Islam, F., DeGrandpre, M., Beatty, C., Krishfield, R., & Toole, J. (2016). Gas exchange of CO₂
1327 and O₂ in partially ice-covered regions of the Arctic Ocean investigated using in situ
1328 sensors. *IOP Conference Series: Earth and Environmental Science*, 35(012018).
1329 <https://doi.org/10.1088/1755-1315/35/1/012018>
- 1330 Ito, T., & Deutsch, C. (2006). Understanding the saturation state of argon in the thermocline: The
1331 role of air-sea gas exchange and diapycnal mixing. *Global Biogeochemical Cycles*, 20(3),
1332 1–15. <https://doi.org/10.1029/2005GB002655>
- 1333 Izett, R., & Tortell, P. (2020). The Pressure of In Situ Gases Instrument (PIGI) for Autonomous
1334 Shipboard Measurement of Dissolved O₂ and N₂ in Surface Ocean Waters. *Oceanography*,
1335 33(2). <https://doi.org/10.5670/oceanog.2020.214>
- 1336 Izett, R., Manning, C. C., Hamme, R. C., & Tortell, P. D. (2018). Refined estimates of net
1337 community production in the Subarctic Northeast Pacific derived from ΔO₂/Ar
1338 measurements with N₂O-based corrections for vertical mixing. *Global Biogeochemical*
1339 *Cycles*, 32, 326–350. <https://doi.org/https://doi.org/10.1002/2017GB005792>
- 1340 Johnson, K. S., Plant, J. N., Dunne, J. P., Talley, L. D., & Sarmiento, J. L. (2017). Annual nitrate
1341 drawdown observed by SOCCOM profiling floats and the relationship to annual net

- 1342 community production. *Journal of Geophysical Research: Oceans*, 122(8), 6668–6683.
1343 <https://doi.org/10.1002/2017JC012839>
- 1344 Jonsson, B. F., Doney, S. C., Dunne, J., & Bender, M. (2013). Evaluation of the Southern Ocean
1345 O₂/Ar-based NCP estimates in a model framework. *Journal of Geophysical Research:*
1346 *Biogeosciences*, 118, 385–399. <https://doi.org/10.1002/jgrg.20032>
- 1347 Juranek, L., Takahashi, T., Mathis, J., & Pickart, R. (2019). Significant Biologically Mediated
1348 CO₂ Uptake in the Pacific Arctic During the Late Open Water Season. *Journal of*
1349 *Geophysical Research: Oceans*, 124(2), 1–23. <https://doi.org/10.1029/2018JC014568>
- 1350 Kaiser, J., Reuer, M. K., Barnett, B., & Bender, M. L. (2005). Marine productivity estimates
1351 from continuous O₂/Ar ratio measurements by membrane inlet mass spectrometry.
1352 *Geophysical Research Letters*, 32(L19605). <https://doi.org/10.1029/2005GL023459>
- 1353 Kalnay, E., Kanamitsu, M., Kistler, R., Collins, W., Deaven, D., Gandin, L., et al. (1996). The
1354 NCEP/NCAR 40-year reanalysis project. *Bulletin of the American Meteorological Society*,
1355 77, 437–471. [https://doi.org/10.1175/1520-0477\(1996\)077<0437:TNYRP>2.0.CO;2](https://doi.org/10.1175/1520-0477(1996)077<0437:TNYRP>2.0.CO;2)
- 1356 Kana, T. M., Sullivan, M. B., Cornwell, J. C., & Groszkowski, K. M. (1998). Denitrification in
1357 estuarine sediments determined by membrane inlet mass spectrometry. *Limnology and*
1358 *Oceanography*, 43(2), 334–339. <https://doi.org/10.4319/lo.1998.43.2.0334>
- 1359 Liang, J.-H. H., Deutsch, C., McWilliams, J. C., Baschek, B., Sullivan, P. P., & Chiba, D.
1360 (2013). Parameterizing bubble-mediated air-sea gas exchange and its effect on ocean
1361 ventilation. *Global Biogeochemical Cycles*, 27(3), 894–905.
1362 <https://doi.org/10.1002/gbc.20080>
- 1363 Liang, J. H., Emerson, S. R., D’Asaro, E. A., McNeil, C. L., Harcourt, R. R., Sullivan, P. P., et
1364 al. (2017). On the role of sea-state in bubble-mediated air-sea gas flux during a winter
1365 storm. *Journal of Geophysical Research: Oceans*, 122(4), 2671–2685.
1366 <https://doi.org/10.1002/2016JC012408>
- 1367 Lockwood, D., Quay, P. D., Kavanaugh, M. T., Juranek, L. W., & Feely, R. A. (2012). High-
1368 resolution estimates of net community production and air-sea CO₂ flux in the northeast
1369 Pacific. *Global Biogeochemical Cycles*, 26(GB4010).
1370 <https://doi.org/10.1029/2012GB004380>
- 1371 Loose, B., & Jenkins, W. J. (2014). The five stable noble gases are sensitive unambiguous tracers
1372 of glacial meltwater. *Geophysical Research Letters*, 41, 2835–2841.
1373 <https://doi.org/doi:10.1002/2013GL058804>
- 1374 Loose, B., McGillis, W. R., Perovich, D., Zappa, C. J., & Schlosser, P. (2014). A parameter
1375 model of gas exchange for the seasonal sea ice zone. *Ocean Science*, 10(1), 17–28.
1376 <https://doi.org/10.5194/os-10-17-2014>
- 1377 Manning, C. C., Stanley, R. H. R., Nicholson, D. P., Loose, B., Lovely, A., Schlosser, P., &
1378 Hatcher, B. G. (2017). Changes in gross oxygen production, net oxygen production, and air-
1379 water gas exchange during seasonal ice melt in the Bras d’Or Lake, a Canadian estuary.
1380 *Biogeosciences Discussions*. <https://doi.org/10.5194/bg-2017-428>
- 1381 McNeil, C., D’Asaro, E., Johnson, B., & Horn, M. (2006a). A gas tension device with response
1382 times of minutes. *Journal of Atmospheric and Oceanic Technology*, 23(11), 1539–1558.

- 1383 <https://doi.org/10.1175/JTECH1974.1>
- 1384 McNeil, C., Katz, D. R., Ward, B., McGillis, W. R., & Johnson, B. D. (2006b). A method to
1385 estimate net community metabolism from profiles of dissolved O₂ and N₂. *Hydrobiologia*,
1386 571(1), 181–190. <https://doi.org/10.1007/s10750-006-0236-7>
- 1387 McNeil, C. L., Johnson, B. D., & Farmer, D. M. (1995). In situ measurement of dissolved
1388 nitrogen and oxygen in the ocean. *Deep-Sea Research Part I*, 42(5), 819–826.
1389 [https://doi.org/10.1016/0967-0637\(95\)97829-W](https://doi.org/10.1016/0967-0637(95)97829-W)
- 1390 Mordy, C. W., Cokelet, E. D., Robertis, A. De, Jenkins, R., Kuhn, C. E., Lawrence-Salvas, N., et
1391 al. (2017). Advances in Ecosystem Research: Saildrone Surveys of Oceanography, Fish,
1392 and Marine Mammals in the Bering Sea. *Oceanography*, 30(2), 113–115.
- 1393 Munro, D. R., Quay, P. D., Juranek, L. W., & Goericke, R. (2013). Biological production rates
1394 off the Southern California coast estimated from triple O₂ isotopes and O₂ : Ar gas ratios.
1395 *Limnology and Oceanography*, 58(4), 1312–1328.
1396 <https://doi.org/10.4319/lo.2013.58.4.1312>
- 1397 Nicholson, D., Emerson, S., Caillon, N., Jouzel, J., & Hamme, R. C. (2010). Constraining
1398 ventilation during deepwater formation using deep ocean measurements of the dissolved gas
1399 ratios 40 Ar/ 36 Ar, N₂ /Ar, and Kr/Ar. *Journal of Geophysical Research*, 115(C11015), 1–
1400 15. <https://doi.org/10.1029/2010jc006152>
- 1401 Nilsson, E. D., Rannik, Ü., Swietlicki, E., Leck, C., Aalto, P. P., Zhou, J., & Norman, M. (2001).
1402 Turbulent aerosol fluxes over the Arctic Ocean 2. Wind-driven sources from the sea.
1403 *Journal of Geophysical Research*, 106(D23), 32139–32154.
- 1404 Palevsky, H. I., Quay, P. D., Lockwood, D. E., & Nicholson, D. P. (2016). The annual cycle of
1405 gross primary production, net community production, and export efficiency across the
1406 North Pacific Ocean. *Global Biogeochemical Cycles*, 30(2), 361–380.
1407 <https://doi.org/10.1002/2015GB005318>
- 1408 Pelland, N. A., Eriksen, C. C., Emerson, S. R., & Cronin, M. F. (2018). Seaglider surveys at
1409 Ocean Station Papa: Oxygen kinematics and upper-ocean metabolism. *Journal of*
1410 *Geophysical Research: Oceans*, 1–20. <https://doi.org/10.1029/2018JC014091>
- 1411 Plant, J. N., Johnson, K. S., Sakamoto, C. M., Jannasch, H. W., Coletti, L. J., Riser, S. C., &
1412 Swift, D. D. (2016). Net community production at Ocean Station Papa observed with nitrate
1413 and oxygen sensors on profiling floats. *Global Biogeochemical Cycles*, 30, 859–879.
1414 <https://doi.org/10.1002/2015GB005349>.Received
- 1415 Reed, A., McNeil, C., D’Asaro, E., Altabet, M., Bourbonnais, A., & Johnson, B. (2018). A gas
1416 tension device for the mesopelagic zone. *Deep-Sea Research Part I*, 139(2018), 68–78.
1417 <https://doi.org/10.1016/j.dsr.2018.07.007>
- 1418 Reynolds, R. W., Smith, T. M., Liu, C., Chelton, D. B., Casey, K. S., & Schlax, M. G. (2007).
1419 Daily High-Resolution-Blended Analyses for Sea Surface Temperature. *Journal of Climate*,
1420 20, 5473–5496.
- 1421 Rosengard, S. Z., Izett, R. W., Burt, W. J., Schuback, N., & Tortell, P. D. (2020). Decoupling of
1422 O₂ / Ar and particulate organic carbon dynamics in nearshore surface ocean waters.
1423 *Biogeosciences*, 17, 3277–3298. Retrieved from <https://doi.org/10.5194/bg-17-3277-2020>

- 1424 Scheifele, B., Waterman, S., Merckelbach, L., & Carpenter, J. R. (2018). Measuring the
1425 Dissipation Rate of Turbulent Kinetic Energy in Strongly Stratified, Low-Energy
1426 Environments: A Case Study From the Arctic Ocean. *Journal of Geophysical Research:
1427 Oceans*, 123, 5459–5480. <https://doi.org/10.1029/2017JC013731>
- 1428 Schmidtko, S., Johnson, G. C., & Lyman, J. M. (2013). MIMOC: A global monthly isopycnal
1429 upper-ocean climatology with mixed layers. *Journal of Geophysical Research: Oceans*,
1430 118, 1658–1672.
- 1431 Shigemitsu, M., Gruber, N., Oka, A., & Yamanaka, Y. (2016). Potential use of the N₂/Ar ratio as
1432 a constraint on the oceanic fixed nitrogen loss. *Global Biogeochemical Cycles*, 30, 576–594.
1433 <https://doi.org/10.1111/1462-2920.13280>
- 1434 Sipler, R. E., Gong, D., Baer, S. E., Sanderson, M. P., Roberts, Q. N., Mulholland, M. R., &
1435 Bronk, D. A. (2017). Preliminary estimates of the contribution of Arctic nitrogen fixation to
1436 the global nitrogen budget. *Limnology and Oceanography Letters*, 2(5), 159–166.
1437 <https://doi.org/10.1002/lol2.10046>
- 1438 Steiner, N., Vagle, S., Denman, K. L., & McNeil, C. (2007). Oxygen and nitrogen cycling in the
1439 northeast Pacific - Simulations and observations at Station Papa in 2003/2004. *Journal of
1440 Marine Research*, 65(3), 441–469. <https://doi.org/10.1357/002224007781567658>
- 1441 Tang, W., Wang, S., Fonseca-Batista, D., Dehairs, F., Gifford, S., Gonzalez, A. G., et al. (2019).
1442 Revisiting the distribution of oceanic N₂ fixation and estimating diazotrophic contribution
1443 to marine production. *Nature Communications*, 10(1), 1–10.
1444 <https://doi.org/10.1038/s41467-019-08640-0>
- 1445 Tang, W., Cerdán-García, E., Berthelot, H., Polyviou, D., Wang, S., Baylay, A., et al. (2020).
1446 New insights into the distributions of nitrogen fixation and diazotrophs revealed by high-
1447 resolution sensing and sampling methods. *ISME Journal*. [https://doi.org/10.1038/s41396-
1448 020-0703-6](https://doi.org/10.1038/s41396-020-0703-6)
- 1449 Teeter, L., Hamme, R. C., Ianson, D., & Bianucci, L. (2018). Accurate Estimation of Net
1450 Community Production From O₂/Ar Measurements. *Global Biogeochemical Cycles*, 1–19.
1451 <https://doi.org/10.1029/2017GB005874>
- 1452 Tengberg, A., Hovdenes, J., Andersson, H. J., Brocandel, O., Diaz, R., Hebert, D., et al. (2006).
1453 Evaluation of a lifetime-based optode to measure oxygen in aquatic systems. *Limnology and
1454 Oceanography: Methods*, 4(2), 7–17. <https://doi.org/10.4319/lom.2006.4.7>
- 1455 Top, Z., Martin, S., & Becker, P. (1988). A laboratory study of dissolved noble gas anomaly due
1456 to ice formation. *Geophysical Research Letters*, 15(8), 796–799.
- 1457 Tortell, P. D. (2005). Dissolved gas measurements in oceanic waters made by membrane inlet
1458 mass spectrometry. *Limnology and Oceanography: Methods*, 3, 24–37.
1459 <https://doi.org/10.4319/lom.2005.3.24>
- 1460 Tortell, P. D., Bittig, H. C., Körtzinger, A., Jones, E. M., & Hoppema, M. (2015). Biological and
1461 physical controls on N₂, O₂, and CO₂ distributions in contrasting Southern Ocean surface
1462 waters. *Global Biogeochemical Cycles*, 29, 994–1013.
1463 <https://doi.org/10.1002/2014GB004975>
- 1464 Ulfso, A., Cassar, N., Korhonen, M., van Heuven, S., Hoppema, M., Kattner, G., & Anderson,

- 1465 L. G. (2014). Late summer net community production in the central Arctic Ocean using
1466 multiple approaches. *Global Biogeochemical Cycles*, 28, 1129–1148.
1467 <https://doi.org/10.1002/2014GB004833>
- 1468 Voermans, J. J., Babanin, A. V., Thomson, J., Smith, M. M., & Shen, H. H. (2019). Wave
1469 Attenuation by Sea Ice Turbulence. *Geophysical Research Letters*, 46(12), 6796–6803.
1470 <https://doi.org/10.1029/2019GL082945>
- 1471 Wang, S., Kranz, S. A., Kelly, T. B., Song, H., Stukel, M. R., & Cassar, N. (2020). Lagrangian
1472 Studies of Net Community Production: The Effect of Diel and Multiday Nonsteady State
1473 Factors and Vertical Fluxes on O₂/Ar in a Dynamic Upwelling Region. *Journal of*
1474 *Geophysical Research: Biogeosciences*, 125(6), 1–19.
1475 <https://doi.org/10.1029/2019jg005569>
- 1476 Wanninkhof, R. (2014). Relationship between wind speed and gas exchange over the ocean
1477 revisited. *Limnology and Oceanography: Methods*, 12(6), 351–362.
1478 <https://doi.org/10.1029/92JC00188>
- 1479 Weeding, B., & Trull, T. W. (2014). Hourly oxygen and total gas tension measurements at the
1480 Southern Ocean Time Series site reveal winter ventilation and spring net community
1481 production. *Journal of Geophysical Research: Oceans*, 119, 348–358.
1482 <https://doi.org/10.1002/2013JC009302>
- 1483 Weiss, R. F. (1970). The solubility of nitrogen, oxygen and argon in water and seawater. *Deep Sea*
1484 *Research*, 17(4), 721–735.
- 1485 Whalen, C. B., Talley, L. D., & MacKinnon, J. A. (2012). Spatial and temporal variability of
1486 global ocean mixing inferred from Argo profiles. *Geophysical Research Letters*, 39(17).
1487 <https://doi.org/10.1029/2012GL053196>
- 1488 Wise, D. L., & Houghton, G. (1966). The diffusion coefficients of ten slightly soluble gases in
1489 water at 10–60°C. *Chemical Engineering Science*, 21(11), 999–1010.
1490 [https://doi.org/10.1016/0009-2509\(66\)85096-0](https://doi.org/10.1016/0009-2509(66)85096-0)
- 1491 Woolf, D. K., & Thorpe, S. A. (1991). Bubbles and the air-sea exchange of gases in near-
1492 saturation conditions. *Journal of Marine Research*, 49, 435–466.
1493 <https://doi.org/10.1357/002224091784995765>
- 1494 Wu, J., Chen, N., Hong, H., Lu, T., Wang, L., & Chen, Z. (2013). Direct measurement of
1495 dissolved N₂ and denitrification along a subtropical river-estuary gradient, China. *Marine*
1496 *Pollution Bulletin*, 66(2013), 125–134. <https://doi.org/10.1016/j.marpolbul.2012.10.020>
- 1497 Yang, B., Emerson, S. R., & Bushinsky, S. M. (2017). Annual net community production in the
1498 subtropical Pacific Ocean from in-situ oxygen measurements on profiling floats. *Global*
1499 *Biogeochemical Cycles*, 31, 728–744. <https://doi.org/10.1002/2016GB005545>
- 1500 Zhou, J., Delille, B., Brabant, F., & Tison, J. L. (2014). Insights into oxygen transport and net
1501 community production in sea ice from oxygen, nitrogen and argon concentrations.
1502 *Biogeosciences*, 11, 5007–5020. <https://doi.org/10.5194/bg-11-5007-2014>
- 1503